Article

Immunity

Microglia-glioblastoma crosstalk mediates glioblastoma invasion at the far infiltration zone

Graphical abstract

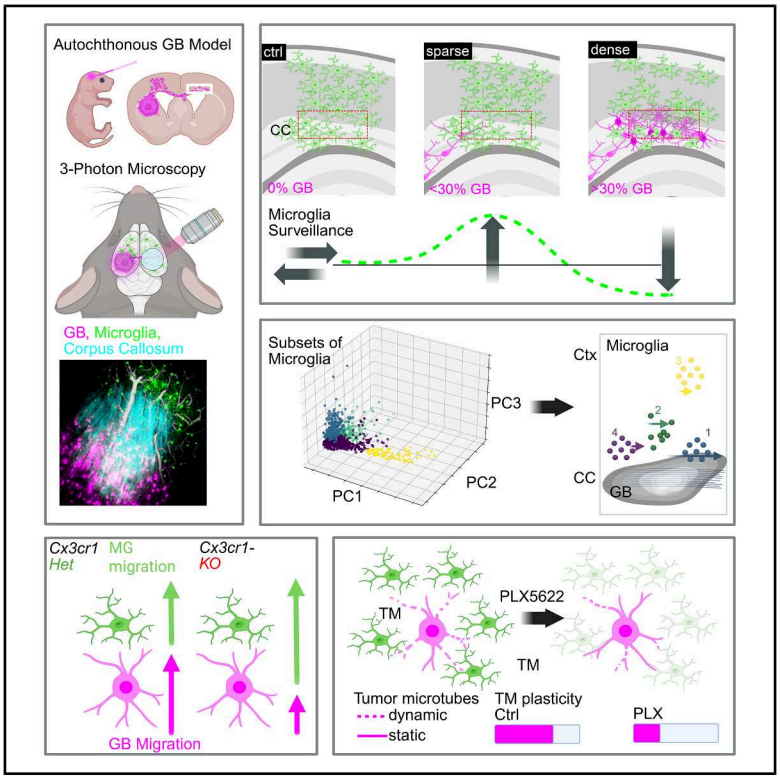

Highlights

- 3-photon microscopy of microglia and glioblastoma at the far infiltration zone
- Microglia show biphasic surveillance during glioblastoma infiltration
- Glioblastoma cell proximity shapes spatial microglial heterogeneity
- Microglia manipulation impairs tumor microtube plasticity and invasion

Authors

Felix C. Nebeling, Falko Fuhrmann, Manuel Mittag, ..., Ulrich Herrlinger, Paolo Salomoni, Martin Fuhrmann

Correspondence

felix.nebeling@dzne.de (F.C.N.), ulrich.herrlinger@ukbonn.de (U.H.), paolo.salomoni@dzne.de (P.S.), martin.fuhrmann@dzne.de (M.F.)

In brief

Infiltration of glioblastoma (GB) cells into the brain parenchyma and colonization of distant regions are associated with disease recurrence and therapy resistance. Using 3-photon intravital microscopy in an autochthonous GB model, Nebeling et al. identify structured, stage-dependent microglial responses at the far infiltration zone and show that microglial manipulation modulates tumor microtube plasticity and invasion.

Nebeling et al., 2026, Immunity *59*, 1075–1091
April 14, 2026
https://doi.org/10.1016/j.immuni.2026.03.010

CellPress

Immunity

CellPress
OPEN ACCESS

Article

Microglia-glioblastoma crosstalk mediates glioblastoma invasion at the far infiltration zone

Felix C. Nebeling,[1,2,15,*] Falko Fuhrmann,[2] Manuel Mittag,[2] Fabrizio Musacchio,[2] Henrike Antony,[2] Nala Gockel,[2] Lea L. Friker,[3,4] Sonia Leonardelli,[4] Severin Filser,[5] Deli A.,[6] Miriam Stork,[6,7] Daniele Bano,[7] Torsten Pietsch,[3] Frank A. Giordano,[8,9,10] Qihui Zhou,[11] Simona Parrinello,[12] Michael Hölzel,[4] Ulrich Herrlinger,[1,14,*] Paolo Salomoni,[6,13,14,*] and Martin Fuhrmann[2,14,*]

[1]Department of Neurooncology, Center for Neurology, University Hospital Bonn, Bonn, Germany
[2]Neuroimmunology and Imaging Group, German Center for Neurodegenerative Diseases (DZNE), Bonn, Germany
[3]Institute of Neuropathology, University Hospital Bonn, University of Bonn, Bonn, Germany
[4]Institute of Experimental Oncology, Medical Faculty, University Hospital Bonn, University of Bonn, Bonn, Germany
[5]Light microscopy facility, German Center for Neurodegenerative Diseases (DZNE), Bonn, Germany
[6]Nuclear Function in CNS Pathology, German Center for Neurodegenerative Diseases (DZNE), Bonn, Germany
[7]Aging and Neurodegeneration, German Center for Neurodegenerative Diseases (DZNE), Bonn, Germany
[8]Department of Radiation Oncology, University Medical Center Mannheim, Mannheim, Germany
[9]DKFZ-Hector Cancer Institute, University Medical Center Mannheim, Mannheim, Germany
[10]Mannheim Institute of Intelligent Systems in Medicine (MIISM), Medical Faculty Mannheim, Heidelberg University, Mannheim, Germany
[11]Adaptive immunity in neurodegeneration, German Center for Neurodegenerative Diseases (DZNE), Munich, Germany
[12]Samantha Dickson Brain Cancer Unit, University College London Cancer Institute, London WC1E 6DD, UK
[13]University College London (UCL) Cancer Institute, Department of Cancer Biology, University College London, London, UK
[14]These authors contributed equally
[15]Lead contact
*Correspondence: felix.nebeling@dzne.de (F.C.N.), ulrich.herrlinger@ukbonn.de (U.H.), paolo.salomoni@dzne.de (P.S.), martin.fuhrmann@dzne.de (M.F.)
https://doi.org/10.1016/j.immuni.2026.03.010

SUMMARY

Glioblastoma (GB) cells infiltrate the brain parenchyma and colonize distant regions, driving recurrence and therapy resistance. Here, we examined dynamic microglial responses to infiltrating tumor cells during GB progression. Three-photon imaging in an autochthonous, immunocompetent GB mouse model enabled visualization of microglia-GB interactions at the far infiltration zone (FIZ) in the corpus callosum (CC). GB infiltration speed varied by anatomical location and tumor microtube (TM) number. Microglia increased surveillance in sparsely infiltrated areas but reduced it with higher GB density, revealing a biphasic response. Directional migration toward GB cells was restricted to microglial subsets within a defined spatial range, indicating heterogeneous reactivity. CX3CR1 deficiency enhanced microglial reactivity while limiting GB cell migration. Microglia depletion with the CSF1R inhibitor PLX5622 reduced GB cell migration and constrained TM plasticity. Thus, microglia respond to GB cell infiltration in a stage-dependent manner and critically modulate dissemination at the FIZ.

INTRODUCTION

Glioblastomas (GBs) are the most common and most malignant primary brain tumors in adults.[1] Despite extensive therapeutic intervention, including surgery, radiotherapy, and chemotherapy, the median survival in unselected trial cohorts remains limited to about 17 months.[2] A major determinant of GB aggressiveness is the diffuse infiltration of adjacent parenchyma (near infiltration zone) and colonization of distant sites (far infiltration zone, FIZ), including the contralateral hemisphere and brainstem.[3–5] Tumor cells at the FIZ are clinically relevant because they evade resection as well as initial radiotherapy and drive recurrence. Accordingly, parenchymal invasion and long-distance colonization are major causes of treatment failure.[3,4,6] The near infiltration zone in mouse models of GB refers to brain regions 0.5–2 mm distal to the tumor bulk that contain infiltrating GB cells.[7,8] Consequently, the FIZ refers to invasion fronts >2 mm away, which change dynamically in space and time. Increasing evidence suggests that GB cells in these tumor niches are functionally distinct.[9–13] Both intrinsic features of GB cells and the surrounding tumor microenvironment (TME) differ between niches.[14,15] GBs develop within a complex microenvironment composed of diverse cell populations, including infiltrating and resident immune cells that may comprise up to 30%–50% of the non-neoplastic compartment.[16,17] Tumor-associated microglia and macrophages can play a tumor-supportive role by releasing factors that promote tumor growth and establish an immunosuppressed microenvironment.[18–21] Indeed, the FIZ may represent a microglia-privileged niche.[15,22–26] However, we lack a comprehensive understanding of microglial dynamics at the FIZ and how they contribute to GB cell migration. Under

physiological conditions, microglia constantly surveil their surroundings with highly plastic fine processes, a phenomenon termed microglial motility,[27,28] which enables them to quickly detect and respond to even subtle microenvironmental changes. Although key drivers of microglial motility have been identified under homeostatic conditions and certain brain pathologies, our understanding of microglial dynamics during GB cell infiltration is limited. Most studies rely on static histology or *in vitro* models and focus on the tumor bulk.[14,18,29] Despite the critical role of infiltrating GB cells in relapse after surgical resection,[30,31] their behavior and features at the FIZ remain insufficiently explored, underscoring the need for *in vivo* studies in this niche.[32–34]

Studying microglial dynamics in relation to GB cells at the FIZ remains challenging due to (1) inaccessibility of deep brain regions to intravital two-photon (2P) microscopy and (2) a lack of faithful GB mouse models. The limitations of commonly used models such as GL261 and patient-derived xenografts (PDXs) include excessive immunogenicity, lack of diffuse infiltration patterns,[35] and incomplete immune system function in PDXs.[36] These shortcomings may explain why many immunotherapeutic drugs successfully tested in preclinical settings later failed in clinical trials.[37–41] Therefore, more representative mouse models that recapitulate both diffuse infiltration and immunogenicity are needed to foster informed GB immunotherapies. Accordingly, we and others have developed autochthonous GB models induced by *in vivo* electroporation, which enable investigation of GB and TME dynamics and the identification of tumor vulnerabilities.[7,42–45] A major route of GB cell infiltration is the *corpus callosum* (CC),[30,46–49] located ~800 μm below the pial surface in adult mice. Conventional 2P microscopy does not permit noninvasive imaging of this anatomical structure, thus precluding investigations of the FIZ.[50] Three-photon (3P) microscopy is a promising tool for deep brain intravital imaging, allowing for noninvasive visualization of cellular structures at depths of 1,100–1,600 μm below the brain surface, depending on the brain area.[51,52] 3P microscopy enabled visualization of GB cells inside the CC and cortex near the ipsilateral tumor bulk in an immunodeficient PDX model.[53]

Here, we applied longitudinal 3P-imaging to a somatic IDH^{WT} mesenchymal (Mes) GB model[7] in immunocompetent mice, focusing on the contralateral CC and cortex, where infiltrating GB cells can be studied in otherwise intact tissue, to avoid potentially confounding changes such as edema, necrosis, or angiogenesis that dominate the tumor bulk and peritumoral zones. We found that in the FIZ, distinct GB morphologies correlate with invasion velocity. Furthermore, microglial motility and movement directionality are differentially regulated by tumor burden. Deficiency of the microglial chemokine receptor CX3CR1 or pharmacological microglia depletion via CSF1R antagonists revealed that microglia are critical for GB cell migration and dissemination at the FIZ. Our findings advance the understanding of how microglia shape GB dissemination and may help identify targetable vulnerabilities in infiltrating tumor niches.

RESULTS

GB cell velocity inversely correlates with TM number at the FIZ

Diffuse infiltration is a hallmark of GB and drives recurrence.[3–5] To study these infiltration patterns within an intact TME, we employed an autochthonous GB model based on *in vivo* electroporation (Figure 1).[7,42–45] We injected a PiggyBac-based plasmid mix encoding a fluorescent reporter, Cas9, and gRNAs targeting Nf1, Trp53, and Pten into the ventricular space at postnatal day two.[54] Upon electroporation, GBs developed in the forebrain, as previously reported.[7,42,45] After 2–3 months, mice developed high-grade diffusely infiltrating gliomas (Figures 1A–1D; Video S1). GB cells reliably infiltrated the contralateral hemisphere via the CC, thereby constituting the FIZ (Figures 1B–1D; Video S1). Tumors recapitulated mesenchymal features, including CD44 enrichment and increased proliferation (Figures 1E and 1F).

To visualize infiltration into deep regions, such as the CC, we carried out 3P *in vivo* imaging in this model. Cranial windows were implanted contralateral to tumor induction, enabling longitudinal imaging of GB cells in the cortex and CC (Figures 2A–2C). Compared with 2P excitation (λ_{Ex} = 920 nm), 3P excitation (λ_{Ex} = 1,300 nm) enabled imaging beyond 1 mm depth, visualizing the CC (Figures 2D and 2E). To delineate white matter architecture, we recorded third-harmonic generation (THG) signals at λ_{Ex} = 1,650 nm excitation (Figures 2F and 2G; Video S2). THG is a label-free nonlinear optical signal generated at refractive index interfaces, providing intrinsic contrast without exogenous fluorophores. Because the lipid-rich myelinated axons of the CC create strong refractive index discontinuities,[55,56] they generate robust THG contrast that enables *in vivo* visualization of white matter architecture. In addition to visualizing axons in the CC, excitation at λ_{Ex} = 1,650 nm also allowed reliable detection of infiltrating $tdTomato^{+}$ GB cells within this region (Figure 2G). We next measured GB cell migration velocity and correlated it with morphological properties of individual GB cells in the CC over several hours (Figures 2H and 2I). Venkataramani et al.[13] demonstrated that GB cell migration velocity near the tumor bulk relates to the abundance of tumor microtubes (TMs).[13,57] TMs are thin protrusions of GB cells that facilitate intercellular connectivity and communication with the surrounding TME.[57,58] In our autochthonous model, we recorded GB cells spreading from the tumor bulk into the contralateral hemisphere through the CC. Similar to GB cells near the tumor bulk, we found that cells in the FIZ with few TMs migrated over longer distances and at higher velocities, whereas GB cells with many TMs traveled shorter distances and moved slower (Figures 2I–2L; Video S3). We also observed a small fraction of GB cells without TMs (TM^0 GB cells), representing only 2.2% of all GB cells (Figure S1A–S1F). These TM^0 GB cells were almost stationary, with an average speed of <2 μm/h (Figure S1C). When we grouped GB cells into those with ≤4 TMs and >4 TMs, cells with fewer TMs traveled significantly longer distances (Figures 2J and 2K). GB cells with ≤4 TMs migrated with a velocity of 15 μm/h, which was 72% faster than cells with >4 TMs (9 μm/h; Figure 2L). Moreover, we identified an inverse correlation between the number of TMs and the distance traveled by GB cells ($r = -0.47$, $p = 0.0006$; Figure 2M).

GB cell infiltration velocity depends on anatomical location

Having established that the TM number influences single-cell migration at the FIZ, we next asked how GB cell migration evolves over consecutive days and whether it differs by anatomical location. We performed repeated 3P microscopy in GB-bearing mice over three to four consecutive days at 24-h

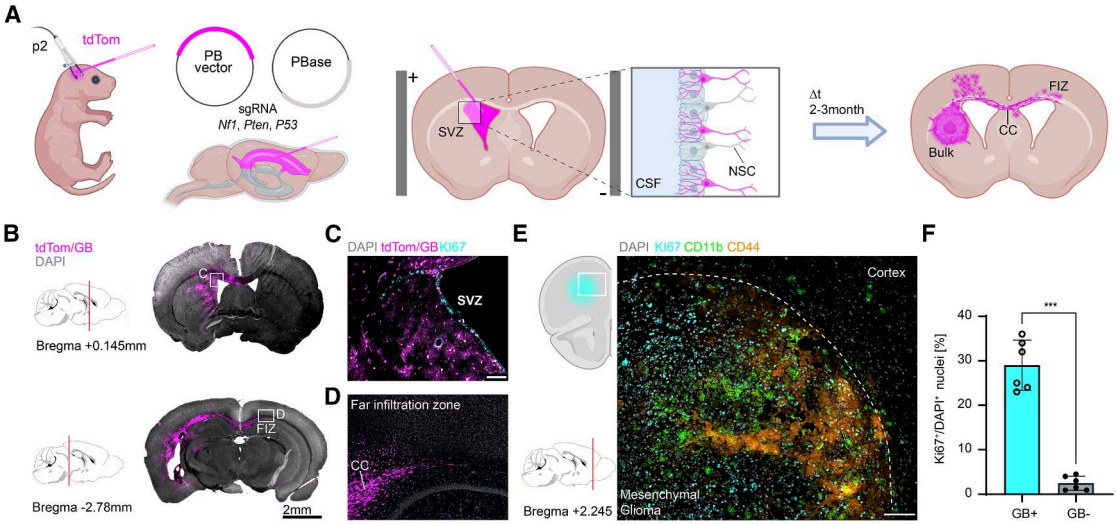

Figure 1. CRISPR-Cas-mediated autochthonous model of adult mesenchymal Glioblastoma

(A) Schematic of CRISPR-Cas-mediated generation of an autochthonous GB model with mesenchymal signature.

(B) Exemplary images showing diffuse infiltration of tdTom+ GB cells in an adult mouse brain (2 months). Note the long-ranging infiltration via the CC crossing to the FIZ of the contralateral hemisphere.

(C and D) Zoom of marked regions in (B) showing the injected subventricular zone (SVZ) (C) and the contralateral CC (D) constituting the FIZ.

(E) Excerpt of the tumor bulk and the near peritumoral tissue highlighting the immunoreactivity for CD44 and CD11c resembling the mesenchymal subtype of human GB.

(F) Quantification of Ki67-positive nuclei inside (GB^+) and outside glioma-bearing tissue (GB^-). n = 6 brain slices from three mice. GB^+ and GB^- areas were quantified in each brain slice.

Data are represented as mean ± SD. ****$p < 0.001$ by unpaired t test.

Scale bars: 2 mm (B, left; C, left), 100 μm (B, left; D), and 50 μm (C, right).

intervals (Figure 3A). Large z stacks spanning ~1 mm covered the entire cortical column and CC (Figure 3B). Recording the same volume repetitively revealed an increase in GB cell density, nearly doubling every 24 h (97% from 0–24 h and 66% from 24–48 h; n_{0h} = 585 ± 171 GB cells/mm^3, n_{24h} = 1,154 ± 357 GB cells/mm^3, n_{48h} = 1,923 ± 634 GB cells/mm^3) (Figure 3, right inset). When comparing anatomical regions, we found that GB cells in the cortex migrated more slowly and covered shorter distances within 24 h than those in the CC (Figures 3C–3E). The mean velocity of GB cells in the CC was ~2-fold higher than in the cortex (Figure 3E). The relative frequency distribution of distances traveled per GB cell revealed two subsets: a predominant slow population (<20 μm/d) and a smaller fast population (up to 100 μm/d) (Figure 3F). In the cortex, most GB cells (87.5% ± 4.5%) belonged to the slow subset (<20 μm/d), whereas in the CC, less than half did (42.8% ± 11.2%). Conversely, fast-migrating GB cells (≥20 μm/d) were more frequent in the CC (57.2% ± 11.2%) than in the cortex (12.5% ± 4.5%) (Figures 3G and 3H). Together, these data demonstrate that GB cells migrate faster and farther within the CC than in the cortex and that migration is heterogeneous, comprising distinct slow and fast subsets. This suggests that spreading GB cells at the FIZ may be shaped by the surrounding tissue context, which modulates their migratory properties.

Microglial surveillance displays a biphasic response to GB cell infiltration

Given that GB cell migration at the FIZ is influenced by the surrounding tissue context, we next examined microglia, the brain's resident immune cells, to assess how they shape and respond to this process. Changes in microglia function and state have been implicated in GB pathogenesis,[18,19,21] and increased $CD68^+$ cell numbers correlate with poor patient prognosis.[59,60] In line with this, we found a significant increase in $CD68^+$ cells within tumor-infiltrated human tissue compared with control regions (38.4% ± 4.5% versus 11.4% ± 1.3%; Figures 4A and 4B). CD68 marks lysosomal activity and is commonly used to identify microglia/macrophages in GB tissue. To move beyond static histology and directly measure microglia-GB dynamics *in vivo*, we focused on the FIZ, a region critical for diffuse invasion and recurrence. GBs were induced in *Cx3cr1*$^{GFP/wt}$ transgenic mice expressing enhanced green fluorescent protein (eGFP) in microglia,[61] enabling visualization of $tdTomato^+$ GB cells alongside GFP^+ microglia during intravital 3P-imaging at the FIZ (Figure 4C). We simultaneously recorded microglia, GB cells, and myelinated CC fibers in a cuboid volume spanning the entire cortex and CC (Figure 4D; Video S4). First, we analyzed morphological parameters of microglia in GB^- and GB^+ regions (Figure 4E). Sholl analysis of microglial ramification revealed reduced branching. Intersections were reduced at increasing radial distances from the soma in GB^+ compared with GB^- samples, indicating shorter and less ramified processes consistent with an amoeboid morphology (Figures 4F and 4G). After determining static morphological differences, we quantified microglial fine process dynamics during GB progression. We compared three different stages of GB cell infiltration within the CC: control, sparse, and dense (0%, <30%, and >30% GB cell coverage; Figure 4H, top). Microglial motility was quantified by acquiring

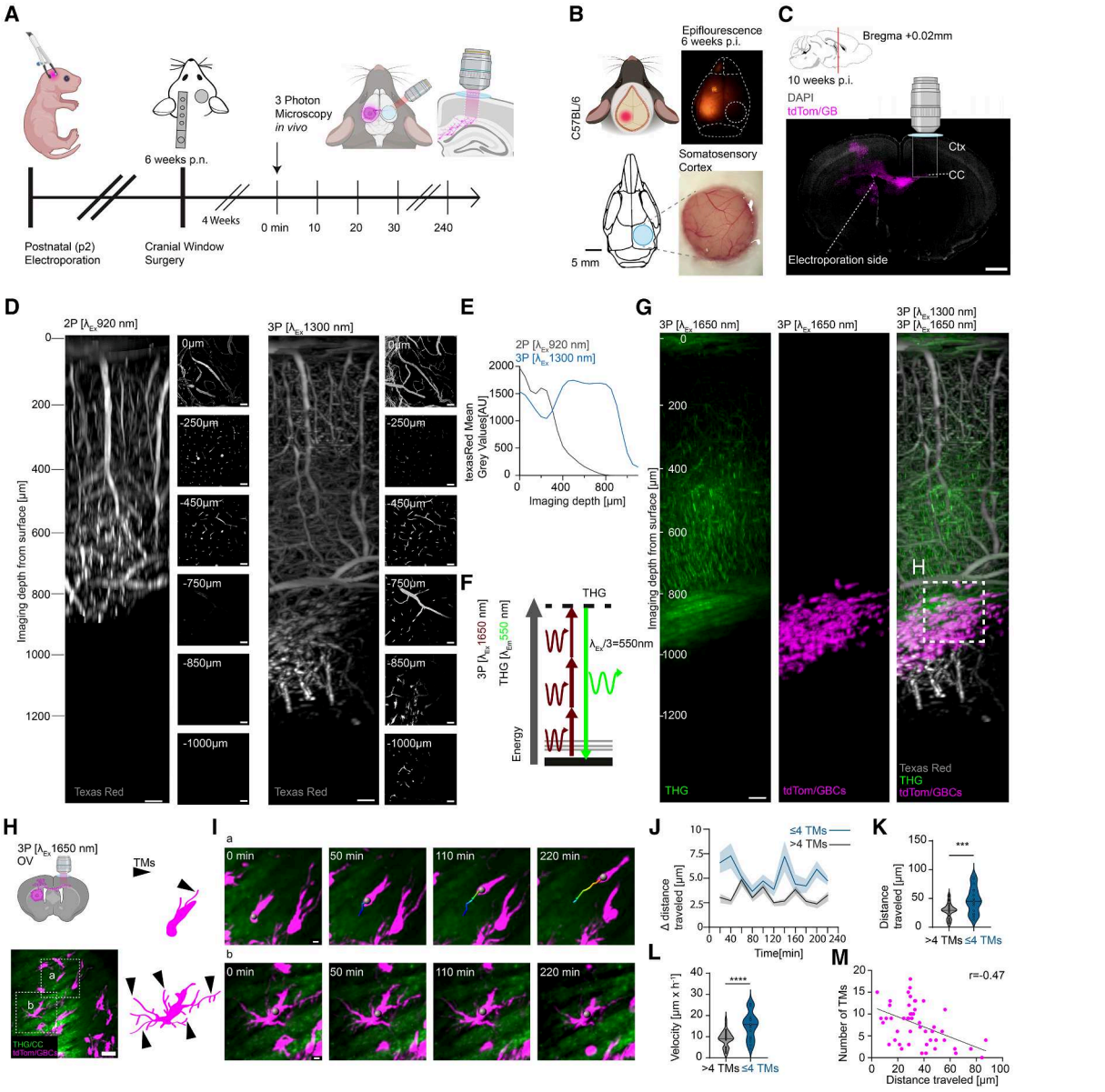

Figure 2. GB cell velocity inversely correlates with the number of TMs at the FIZ

(A) Schematic timeline of the experimental procedure.
(B and C) Localization, window implantation, and CC (CC) imaging position.
(D) Two- versus three-photon excitation of Texas-red labeled blood vessels.
(E) Quantification of mean Texas Red intensity at increasing imaging depths.
(F) Fluorescence generated with third harmonic generation (THG).
(G) Three-photon excitation to visualize CC, GB cells, and blood vessels.
(H) GB cells at the FIZ show different morphologies with low and high numbers of TMs.
(I) Exemplary migration of a GB cell with few TMs (rod-like shape, top) and many TMs (bottom).
(J) GB cells traveled distances plotted over individual time points, >4TMs gray, $\leq$4 TMs blue.
(K and L) Average traveled distance and velocity comparing GB cells with different TM numbers (n = 32 cells > 4TMs and n = 17 cells $\leq$ 4TMs from 3 mice).
(M) Correlation of traveled distance of GB cells during a 3h imaging period and their number of TMs; n = 49 cells; Pearson's $r = -0.47$, $R^2 = 0.22$, $p = 0.0006$.
Violin plots depict the full data distribution (KDE); the line indicates the median. ***$p < 0.001$, ****$p < 0.0001$ by unpaired t test (K and L), Pearson correlation (M).
Scale bars: 500 µm (C), 100 µm (D, overviews), 50 µm (D and H), and 10 µm (I).

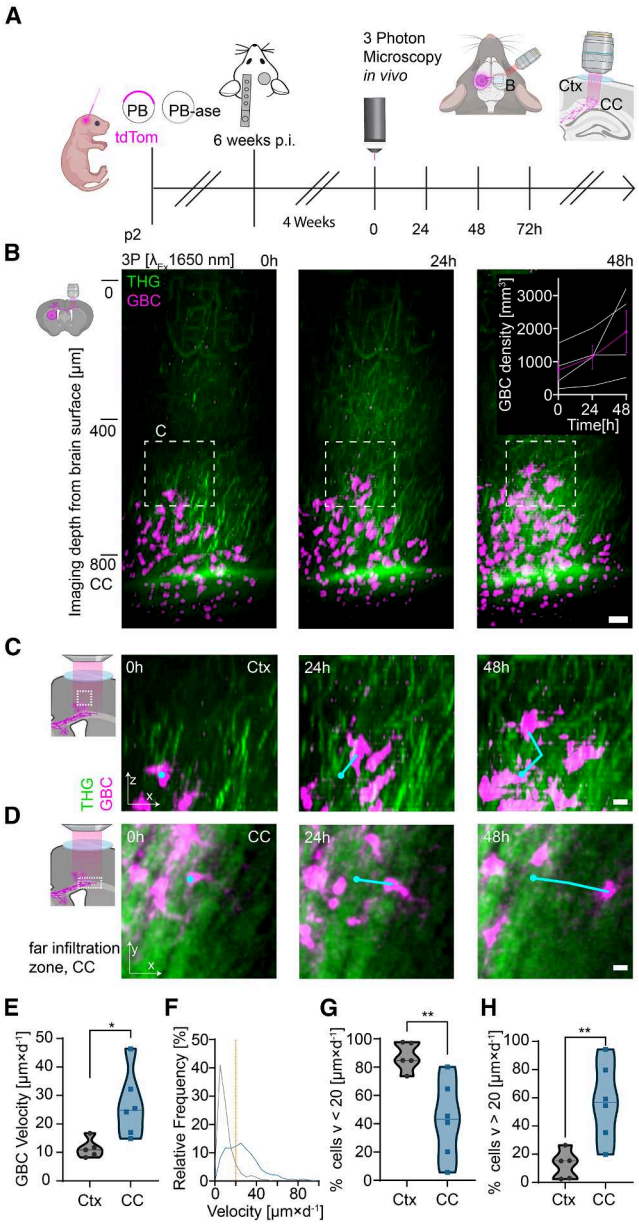

Figure 3. GB cell infiltration velocity depends on anatomical location

(A) Schematic timeline of the experimental procedure.

(B) Side view of a z volume of the contralateral hemisphere with respect to the tumor bulk. Within 48 h, GB cell density increased, nearly doubling per 24 h (inset right).

(C and D) Exemplary images of GB cells migrating inside the cortex (C) and CC (D) at the FIZ.

(E) Velocity of GB cells in the cortex compared with CC (CTX: $n = 5$ and CC: $n = 6$ mice).

(F) Relative frequency distribution of cortical and CC-associated GB cells in relation to their 24 h velocity. Cell movement was binned to 5 µm units (CTX: $n = 614$ and CC: n = 538 GB cells from $n_{Ctx} = 5$ and $n_{CC} = 6$ mice).

(G and H) Comparison of percentage of GB cells in cortex versus CC with a velocity of <20 µm/d (G) and >20 µm/d (H). (CTX $n = 5$ mice and CC $n = 6$ mice). Violin plots depict the full data distribution; the line indicates the median. * $p < 0.05$, ** $p < 0.01$ by unpaired t test (E, G, and H).

Scale bars: 50 µm (B) and 20 µm (C and D).

z-stacks every 5 min across a 150 µm span of the CC (Figure 4H; Video S5). Microglial process turnover rate (TOR) (Figure 4I), as well as gained, lost, and stable fractions, were calculated as previously described.[62,63] In the absence of GB cells, microglial processes displayed an average TOR of 40% ± 1.2%. Upon sparse infiltration, microglia significantly increased surveillance by 17% relative to baseline (Figure 4J). In contrast, under dense infiltration, microglial surveillance decreased by 25% (Figure 4J). The reduced surveillance in dense infiltration was driven by an increase in stable processes and a decrease in gained processes. Conversely, the increase during sparse infiltration was driven by a higher gained fraction together with reduced process stability (Figures 4K and 4L). The loss fractions did not differ between the three groups (Figure 4M). Moreover, we found a marked increase in microglia density in the densely GB cell-infiltrated CC (Figure 4N). Our longitudinal analysis further showed that GB cells progressively populate the CC-adjacent cortex upon sustained GB cell migration to the FIZ in the contralateral hemisphere. Infiltration of the cortex was accompanied by microglia adopting an amoeboid shape with reduced branching (Figures S2A–S2E). Whereas microglial surveillance was unchanged under sparse infiltration, it markedly decreased under dense infiltration conditions (Figures S2F–S2H), reflecting increased process stability and reduced dynamic remodeling (Figures S2I–S2K). Microglia density also increased substantially under dense GB cell infiltration (Figure S2L). Together, these data reveal a biphasic microglial response to GB infiltration, characterized by an early increase in surveillance followed by suppression under dense infiltration, with distinct dynamics in white versus gray matter.

Identification of microglia subsets with distinct migration properties in relation to GB cell infiltration

Microglia have been proposed to accumulate at GB infiltration zones,[22,23,26] yet their behavior at the FIZ has not been quantified longitudinally. We therefore repeatedly recorded the same contralateral somatosensory cortex and CC at 24-h intervals over several days using 3P microscopy (Figures 5A and 5B). Large z-volumes (~1,000 µm) spanning the entire cortical column and CC were acquired (Figure 5C), enabling analysis of microglial migration across depths and distances from invading GB cells. We found that microglia residing in GB cell-free cortical areas remained stationary over time and did not exhibit significant migratory behavior (Figure 5D; Video S6). In contrast, microglial migration increased in close proximity to GB cells infiltrating along the CC into the contralateral hemisphere (Figures 5E and 5F; Video S6). Furthermore, microglia traveled 2.4-fold longer distances when located within 150 µm of the nearest GB cell compared with more distant microglia (Figures 5F and 5G). Consistently, microglia in non-infiltrated cortex exhibited lower variance in Euclidean nearest-neighbor distances compared with microglia in the CC at the FIZ (Figure 5H). Because microglia can display heterogeneous responses even when located in close proximity,[64,65] we next asked whether such heterogeneity was also reflected in their migratory behavior. To this end, we performed unbiased agglomerative hierarchical clustering to group microglia based on similarities across multiple migration features, without predefined categories. Principal component analysis identified subsets with distinct migratory properties.

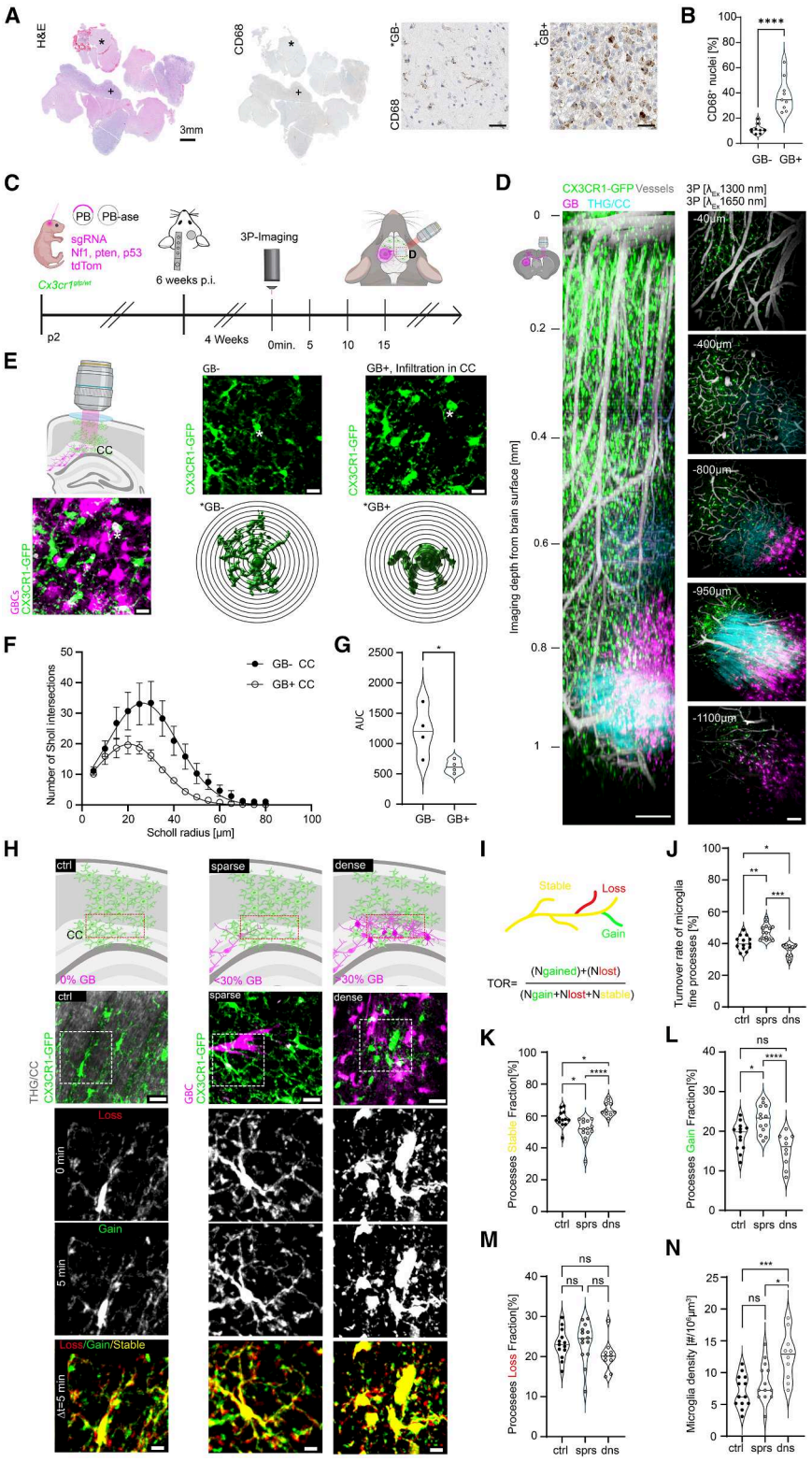

Figure 4. Microglial surveillance displays a biphasic response to GB cell infiltration at the FIZ

(A) Overview of human glioblastoma FFPE consecutive resection samples stained with H&E and against KP1 (CD68), showcasing GB$^+$ (+) and non-infiltrated zones (*). Right panels show the respective zoom images of CD68$^+$ cells.

(B) Percent CD68$^+$ of hematoxylin-stained nuclei in GB$^+$ and GB$^-$ tissue. (n = 9 brain slices from three patients). GB$^+$ and GB$^-$ areas were quantified in each brain slice.

(C) Schematic of the experimental timeline to visualize microglia and GB cells.

(D) 3D reconstruction of a z stack spanning ~1,150 µm containing cortex and CC at the FIZ (microglia [green], vessels [gray], GB cells [magenta], CC/THG [cyan]). Right: x,y images with cellular resolution at different imaging depths.

(E) Representative images of microglia in CC in GB$^-$ or GB$^+$ CC. Asterisks indicate representative 3D reconstructions of individual microglia for Sholl analysis (bottom).

(F and G) Sholl intersection profile (F) and area under curve (AUC) (G) of microglia comparing GB$^-$ and GB$^+$ conditions (n = 4 mice per group).

(H) Schematic (top) and representative images of microglia (green) and their processes for three different stages of GB cell (magenta) progression within the CC: ctrl, sparse, and dense (0%, <30%, and >30% GB coverage). Lower three panels: subsequent time points (0 min, 5 min) were superimposed (Δt = 5 min) to measure gained (green), lost (red), and stable (yellow) processes.

(I) Schematic explaining microglial turnover rate (TOR) as readout for process motility.

(J–N) TOR of microglial fine processes comparing ctrl, sparse, and dense GB infiltration (J); fraction of stable, gained, and lost microglial processes (K–M); and microglia density (N). (J–N: n = 13 ctrl, 14 sparse, 10 dense FOVs in n = 5 ctrl, 7 sparse, 3 dense mice.)

Violin plots depict the full data distribution; line indicates the median. $^*p < 0.05$, $^{**}p < 0.01$, $^{***}p < 0.001$, $^{****}p < 0.0001$, ns $p > 0.05$ by unpaired t test (B), unpaired t test (F and G), and one-way ANOVA with Šídák's multiple comparison test (J–N).

Scale bars: 3 mm (A), 200 µm (D, left), 100 µm (D, right), 20 µm (E and H, second horizontal panel), and 10 µm (H, bottom).

We analyzed sub-volumes of our imaging stacks: horizontal sub-volumes spanning the XY plane (Figures 5C–5E and 5I–5M) and vertical sub-volumes spanning the entire Z-dimension (restricted in XY to 100 µm windows; Figures 5C, 5F, and 5N–5R). Within horizontal volumes, we identified four microglial subsets primarily distinguished by tumor proximity and migratory behavior (Figures 5J–5M). Notably, microglia in Cluster 1 ($C_{XY}1$), located within the CC in close proximity to GB cells, exhibited increased migration distances, consistent with proximity-dependent activation. In contrast, distant cortical subsets ($C_{XY}3$) remained largely sessile. To determine whether the proximity-dependent heterogeneity of microglial subsets at the FIZ

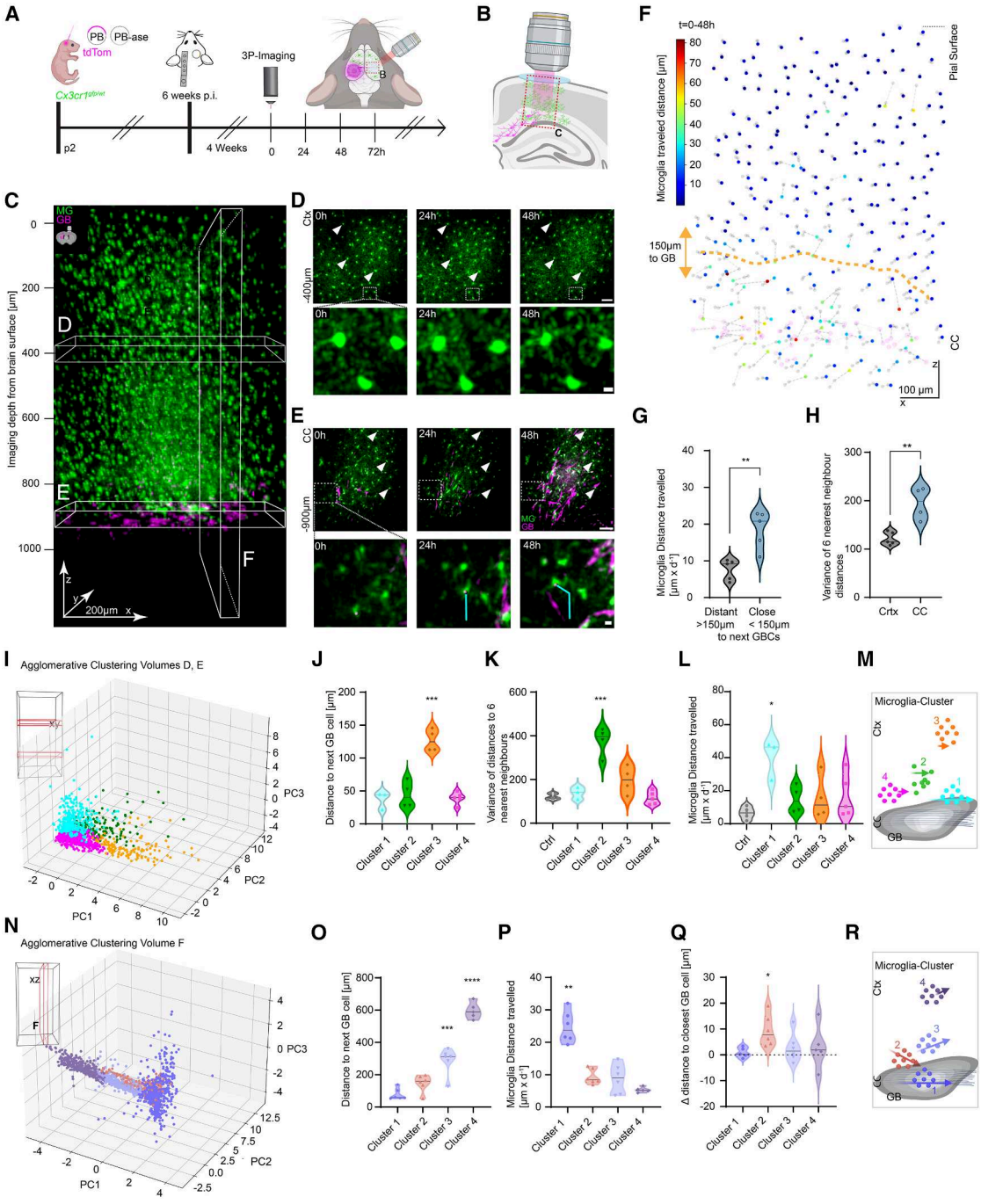

Figure 5. Microglia subsets differ by their migration properties towards invading tumor cells

(A and B) Schematic illustration of the experimental timeline (A) and imaging at the FIZ (B).

(C) 3D side projection of microglia (green) through the entire cortex and into CC harboring migrating GB cells (magenta).

(D) Cortical microglia from the region labeled in (C) in the absence of GB cells were imaged over 48 h. Arrows indicate stationary microglia. Bottom: zoom.

(E) Microglia in CC from the labeled region in (C) depicting an early GB infiltration time point. Arrows indicate stationary microglia. Bottom: zoom showing microglia migration (cyan trajectory).

(F) Visualization of an *x*,*z*-dimension sub-volume as indicated in (C), in which individual microglia are displayed as dots with a color coding from blue to red depending on their traveled distances over 48 h. The migration direction of each microglia is displayed as a dashed line. GB cells (magenta) within the CC. The orange dashed line indicates a 150 µm perimeter around infiltrating GB cells.

(G) Microglia traveled distances per day at >150 or <150 µm range to the next GB cell (n = 5 mice).

(H) Variances of six nearest neighbors of microglia comparing CTX and CC (CTX n = 5 and CC n = 4 mice).

(I) 3D principal component analysis (PCA) reveals 4 distinct sub-groups of microglia in *x*,*y*-volumes (n = 1,055 cells).

(legend continued on next page)

identified in horizontal volumes was maintained across cortical depth, we applied the same clustering strategy to vertical subvolumes (Figure 5N). Vertical clustering confirmed a similar organizational principle. Microglia located within tumor-infiltrated regions (C_Z1) exhibited increased traveled distances but moved non-directionally, whereas cortical microglia (C_Z4) remained largely sessile. Importantly, only the C_Z2 subset displayed directed migration toward GB cells, reflected by a consistent reduction in distance to the nearest tumor cell (Figures 5O–5R). Together, these data demonstrate proximity-dependent heterogeneity of microglial migratory phenotypes at the FIZ.

CX3CR1-deficiency decreases tumor growth and GB cell velocity

We next investigated potential mechanisms underlying microglia-GB cell interactions, focusing on chemokine signaling via CX3CR1, a microglial receptor regulating homeostasis and migration.[62,66,67] GBs were induced in heterozygous *Cx3cr1*$^{gfp/wt}$ and homozygous CX3CR1-deficient *Cx3cr1*$^{gfp/gfp}$ littermates (Figure 6A). After localizing the FIZ by THG/CC signal and GB cell presence (Figure 6B), we quantified GB cell densities over three consecutive days (Figure 6C). GB cell expansion was attenuated in CX3CR1-deficient mice, with density increases of 44% versus 26% at day 1% and 94% versus 41% at day 2 in *Cx3cr1*$^{gfp/wt}$ and *Cx3cr1*$^{gfp/gfp}$, respectively (Figure 6D). By tracking individual microglia and GB cells over three days, we found that CX3CR1-deficient microglia migrated 71% faster than in *Cx3cr1*$^{gfp/wt}$ mice, whereas GB cells showed a 29% reduced velocity (Figures 6E–6I; Video S7). To determine whether the altered migration velocity of microglia was accompanied by changes in local surveillance, we analyzed microglial process turnover across control, sparse, and dense GB infiltration stages (Figure 6J). In *Cx3cr1*$^{gfp/wt}$ mice, microglial fine process motility showed a biphasic pattern, with turnover increasing (+18%) from control to sparse GB infiltration and decreasing (−29%) from sparse to dense GB stages (Figure 6K). These changes were consistent with our earlier observations (Figure 4J). In contrast, in *Cx3cr1*$^{gfp/gfp}$ mice, microglia did not exhibit an initial motility increase upon sparse infiltration (+1%) but showed a decline of ∼15% in dense conditions (Figure 6K). Baseline microglial fine process turnover did not differ between genotypes, indicating that CX3CR1 deficiency primarily altered dynamic responses to GB infiltration rather than intrinsic surveillance capacity. Since microglia have a high phagocytic capacity, we examined whether this correlated with reduced GB cell expansion and migration in *Cx3cr1*$^{gfp/gfp}$ mice. We quantified phagocytic structures (Figure 6L) as morphological correlates of engulfment activity.[68–72] These structures appeared as small, cup-like or bulbous microglial protrusions associated with ongoing or recent phagocytosis and measured 10.2 ± 3.6 μm in diameter. The number increased with the GB-infiltration stage in microglia of both genotypes. However, CX3CR1-deficient microglia had 2.2-fold more phagocytic structures at sparse and 3-fold more at dense GB-infiltration stages than microglia in *Cx3cr1*$^{gfp/wt}$ mice (Figure 6M). Whereas control heterozygous microglia showed a moderate correlation between microglial fine process motility and number of phagocytic structures (Figure S3A), this correlation was absent in *Cx3cr1*$^{gfp/gfp}$ mice (Figure S3B). Importantly, microglial density increased similarly in both genotypes across stages, excluding cell numbers as a confounding factor (Figure S3C). These findings indicate that CX3CR1 deficiency enhances microglial migration over days and increases their reactivity in our GB mouse model, as reflected by persistently elevated phagocytic structures, whereas fine process motility remained unchanged. These alterations were accompanied by reduced GB cell expansion and migration at the FIZ, suggesting that CX3CR1 signaling contributes to microglial engagement with infiltrating GB cells and influences GB dynamics within this critical niche.

CSF1R-mediated microglia reduction reduces GB cell migration and TM plasticity

To further define the contribution of microglia to GB cell invasion at the FIZ, we depleted microglia using the CSF1R inhibitor PLX5622. CSF1R signaling is required for microglial survival, and its pharmacological inhibition with PLX5622 reliably reduces microglial numbers *in vivo*.[73] Although CSF1R inhibition has been reported to influence GB growth,[74] its effect on the dynamic behavior of infiltrating GB cells at the FIZ remains unclear. Because TM remodeling is critical for GB cell connectivity and long-range infiltration, we examined whether microglia depletion alters TM plasticity at the FIZ. We induced GBs in *Cx3cr1*$^{gfp/wt}$ mice, implanted cranial windows as described previously, and performed baseline 3P-imaging prior to microglia depletion. We monitored GB cell migration over several days and TM plasticity at the FIZ (Figure 7A). Microglial densities were measured before as well as at 7 and 14 days after initiation of PLX5622 treatment, which resulted in a 76% reduction in microglia (Figures 7B and 7C). At the same time, GB cell density remained unchanged irrespective of the presence of microglia (Figures 7D and 7F). However, microglia depletion significantly reduced the migration velocity of GB cells in comparison with baseline (−62%) and control-treated mice (−57%) (Figures 7E and 7F). The absence of microglia particularly affected the fraction of fast-migrating GB cells (>55 μm/48 h), which decreased by ∼76% (Figures 7G and 7I). As GB migration depends on dynamic

(J–L) Distance to next GB cell (J), distance variance between 6 nearest neighbors (K), and traveled distance (L) of microglia comparing the four subgroups (C1: n = 3, C2, C3: n = 4, C4: n = 5, ctrl = 5 mice).

(M) Schematic visualization of the 4 clusters with respect to their relative distance to the next GB cells, their variance in distances amongst each other, and their respective traveled distances, depicted by the arrow length.

(N) 3D PCA showing 4 distinct subgroups of microglia found in the data obtained from x,z-volumes (n = 1,328 cells).

(O–Q) Distance to next GB cell (O), traveled distance (P), and change (Δ) in distance to closest GB cell (Q) of microglia, comparing the four subgroups (O: C1–C3: n = 6, C4: n = 5 mice; numbers in P as in O; Q: C1 n = 5, rest as in O and P).

(R) Schematic visualization of the 4 clusters with respect to their distance to the next GB cell, traveled distance, and Δ-distance to GB cell depicted by the arrow length and orientation.

Violin plots depict the full data distribution; line indicates the median. *p < 0.05, **p < 0.01, ***p < 0.001, ****p < 0.0001 by unpaired t test (G and H), one-way ANOVA (J–L, O, and P), Kruskal-Wallis (Q).

Scale bars: 50 μm (D, E, and overviews), 10 μm (E, lower), and 5 μm (D, lower).

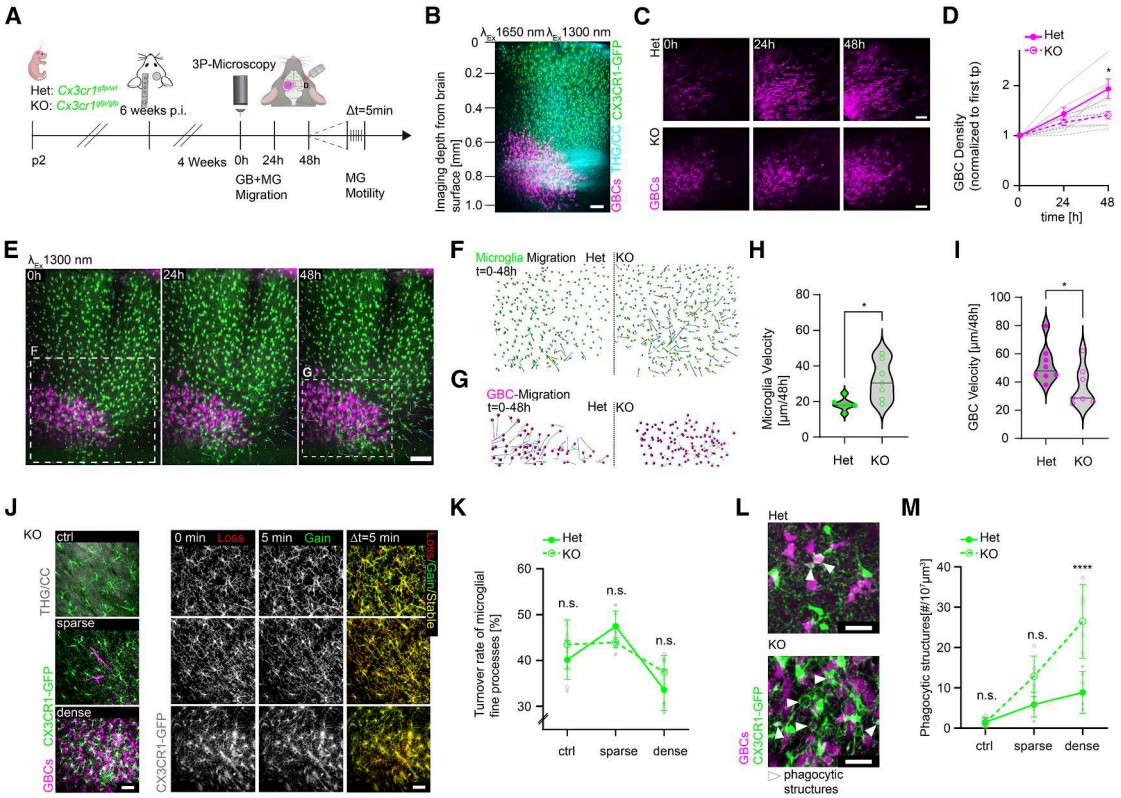

Figure 6. CX3CR1 deficiency alters microglial reactivity to infiltrating GB cells

(A) Schematic of the experimental timeline.

(B) 3D *x*,*z*-projection of the FIZ with microglia (green), GB cells (magenta), and CC (cyan).

(C) Time lapse of GB cells over 48 h in the CC comparing *Cx3cr1*$^{gfp/wt}$ (Het) and *Cx3cr1*$^{gfp/gfp}$ (KO).

(D) Changes in GB cell density over 48 h comparing Het and KO mice (n = 6 mice per group). Mean ± SEM.

(E) Time-lapse *x*,*z*-projections over 48 h of volumes covering the cortical column and CC.

(F and G) Individual microglia (F) and GB cells (G) of insets in (E) were tracked in Imaris (spheres), enabling the generation of migratory tracks for each cell. Examples of Het (left) and KO (right) comparing microglia (F) and GB cells (G).

(H) Microglia velocity comparing Het and KO mice (n = 6 Het and n = 7 KO mice).

(I) Velocity of GB cells in Het and KO recipient mice (n = 8 Het and n = 7 KO mice).

(J) Representative images of microglia and their fine process turnover at distinct GB progression stages (ctrl, sparse, dense). Left: THG (gray), microglia (green), and GB cells (magenta). Right: Subsequent time points (0 min, 5 min) were superimposed (Δt = 5 min) to measure gained (green), lost (red), and stable (yellow) processes.

(K) Turnover rate of microglial fine processes as a measure of their surveillance activity (i.e., microglial motility) across GB-infiltration stages in Het versus KO recipient mice (ctrl: $n_{He\ t}$ = 5, n_{KO} = 5; sparse n_{Het} = 7, n_{KO} = 6; dense n_{Het} = 6, n_{KO} = 8 mice). Mean ± SEM.

(L) Examples of phagocytic structures (arrows) in microglia comparing Het and KO mice.

(M) Density of phagocytic structures comparing Het and KO mice for ctrl (n_{Het} = 6, n_{KO} = 5), sparse (n_{Het} = 6, n_{KO} = 6), and dense (n_{Het} = 5, n_{KO} = 7) GB cell infiltration conditions mean ± SD.

Violin plots (H and I) depict the full data distribution; line indicates the median. n.s. not significant, * $p < 0.05$, ** $p < 0.01$, *** $p < 0.001$, **** $p < 0.0001$ by *t* test (H and I), two-way repeated measures ANOVA (D), two-way ANOVA (K and M).

Scale bars: 100 μm (B and E), 50 μm (C and J), and 20 μm (L).

remodeling of TMs,[13,57,75] we next quantified TM plasticity at the FIZ. Longitudinal 3P imaging revealed dynamic TM remodeling (Figure 7J; Video S8). However, the Euclidean distance to nearby microglia did not correlate with TM dynamics (Figures S4A and S4B), suggesting that proximity to microglia is not sufficient to modulate TM dynamics. We therefore quantified TM plasticity in the absence of microglia (Figure 7K). At baseline, before microglia depletion, TM turnover values were comparable between groups (Ctrl: 32.6% ± 2.0% versus PLX: 35.5% ± 1.5%). In control-treated mice, TM turnover remained essentially stable over two weeks (~2% change). In contrast, TM turnover decreased by ~25% in the absence of microglia over the two-week period (Figure 7L; Video S8). Together, these results suggest that microglia support GB cell migration and TM plasticity at the FIZ, pointing to targetable vulnerabilities within the microglia-GB axis that may be leveraged to modulate tumor invasion.

DISCUSSION

In this study, we combined longitudinal 3P imaging with an immunocompetent autochthonous GB model to characterize microglia-tumor interactions at the FIZ and identified a biphasic

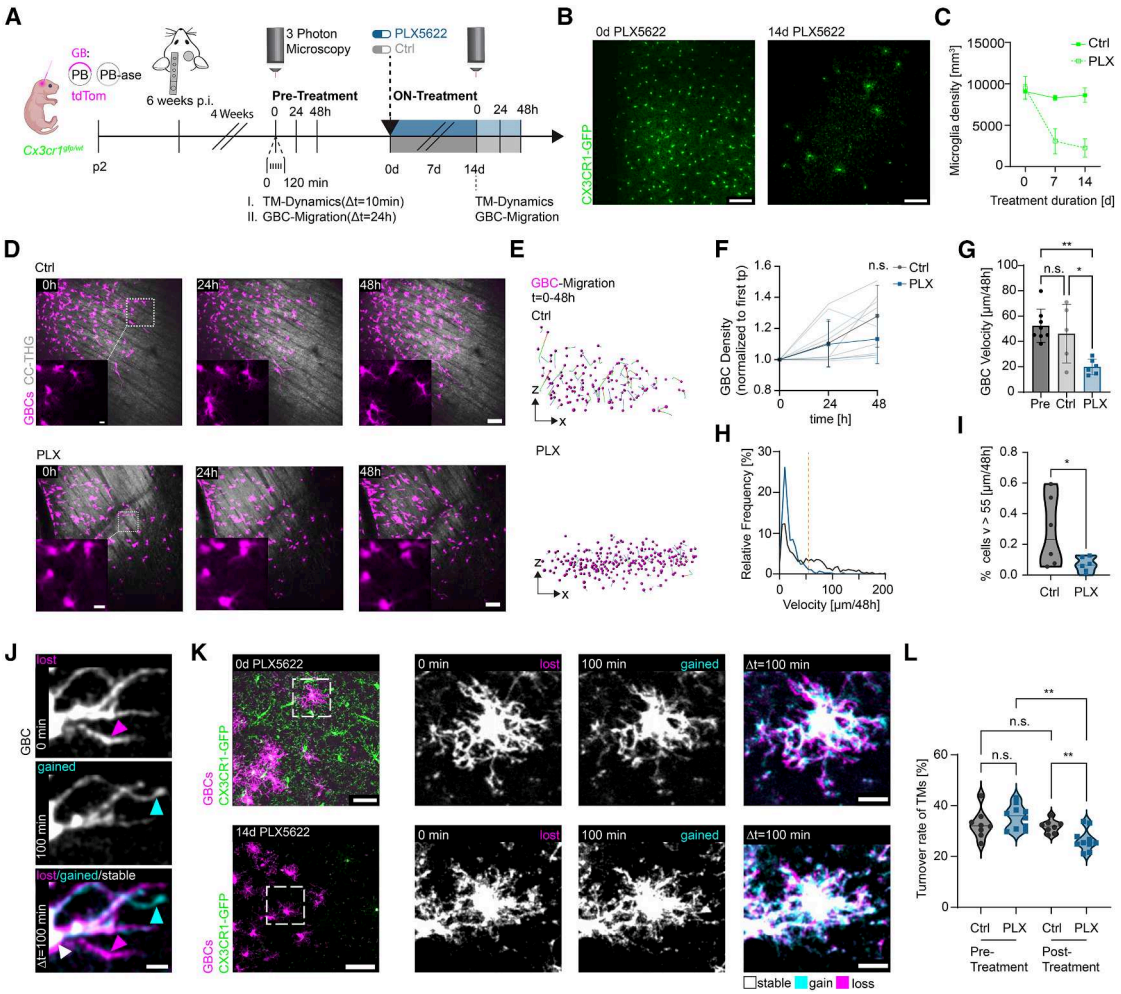

Figure 7. CSF1R inhibition decreases GB cell migration and TM plasticity

(A) Schematic of the experimental timeline.

(B) Exemplary images of microglia in a *Cx3cr1*$^{gfp/wt}$ mouse at 0 and 14 days of PLX5622 treatment.

(C) Microglia density measured at three time points (0, 7, and 14 days of treatment). (Ctrl $n = 5$, PLX $n = 6$ mice)

(D) Time-lapse images over 48 h of GB cells (magenta) within CC (gray) of the FIZ comparing ctrl and PLX-treated mice. Insets: zoom of GB cells.

(E) Exemplary GB cell trajectories (0–48 h) of Ctrl and PLX-treated mice.

(F) Normalized changes in GB cell density within the imaged volume over 48 h ($n = 5$ mice/group).

(G) GB cell velocity prior to treatment (Pre), after 14 days of control diet, and 14 days of PLX. (Pre $n = 8$, Ctrl $n = 5$, PLX $n = 6$).

(H) Relative frequency distribution of GB cell velocity. Cell movement was binned to 5 µm units. ($n = 812$ (ctrl) and $n = 754$ (PLX) GB cells from $n = 6$ mice per group).

(I) Percentage of GB cells with an average velocity of more than 55 µm/48h comparing control (Ctrl) and PLX-treated (PLX) mice ($n = 6$ mice Ctrl and $n = 6$ PLX).

(J) Example of a GB cell at the FIZ. Two time points (Δt 100 min) were pseudo-colored and overlaid (t_0 = magenta, t_0 + 100 min = cyan) to visualize TM plasticity. Magenta segments indicate TMs present at t_0 but retracted by t_0 + 100 min; cyan segments denote newly extended TMs; magenta/cyan overlap appears white, indicating stable segments.

(K) Exemplary images of pre- and post-14 d PLX5622 treatment showing GB cells (magenta) and microglia (green) on the left. Right: two time points (0, 100 min) and their respective pseudo-colored overlay (t_0 = magenta, t_0 + 100 min = cyan).

(L) TM turnover before (pre) and after (post) PLX treatment comparing controls (Ctrl, vehicle-treated) and (PLX, PLX5622-treated) mice (Ctrl $n = 8$ and PLX $n = 10$ mice).

Violin plots (I and L) depict the full data distribution; line indicates the median. Other data are represented as mean ± SD. n.s. not significant, * $p < 0.05$, ** $p < 0.01$, *** $p < 0.001$, **** $p < 0.0001$ by one-way ANOVA (C, F, and G), unpaired *t* test (I), two-way ANOVA followed by Holm-Šídák post hoc test (L).

Scale bars: 200 µm (B), 100 µm (D, overviews), 50 µm (K, left), 40 µm (D, upper inset), 20 µm (D, lower inset; K, right), and 5 µm (J).

surveillance response, heterogeneous migratory phenotypes, and CX3CR1- and CSF1R-dependent effects on GB dissemination. The diffuse nature of GBs and their aberrant TME remain major therapeutic barriers, and the limited translational success of immunotherapies underscores shortcomings of existing preclinical models.[76,77] Xenografts lack immune competence, and commonly used syngeneic models such as GL261 incompletely reflect human disease biology. To overcome limited access to distant infiltration zones, we carried out 3P intravital microscopy in an autochthonous immunocompetent GB model[7,45] to visualize FIZ within

intact CC white matter. We first investigated the relationship between TMs and GB cell migration. TMs are long, thin protrusions that integrate GB cells into multicellular networks,[58,78] conferring resilience against multimodal treatment regimens.[57,75,79] Networked GB cells display ramified morphologies, whereas infiltration is driven by less connected cells.[13] Previous 3P microscopy described TM dynamics near the tumor bulk.[53] We found a large fraction of fast-migrating GB cells in the CC, in contrast to GB cells in the cortex that were primarily stationary. Our findings demonstrate an inverse correlation between TM abundance and GB cell migration velocity at the FIZ, consistent with observations near the tumor bulk. TM abundance may therefore restrain migratory behavior while promoting network integration. Importantly, we and others have shown that targeting TMs disrupts tumor connectivity and represents a potential therapeutic strategy.[80,81] However, our findings indicate that reducing TM connectivity may enhance the migratory capacity of individual tumor cells. We found that GB cells migrate faster in the CC than in the cortex, potentially reflecting differences in extracellular matrix composition. Although the myelin-enriched CC contains migration-inhibiting proteins such as Nogo-A and myelin-associated glycoprotein, GB cells express proteases capable of cleaving these molecules, thereby potentially converting the CC into a permissive migratory scaffold.[82] Within the non-neoplastic TME, microglia constitute up to ~30% of the tumor bulk and closely interact with GB cells. However, their pro- or anti-tumor roles remain incompletely understood, likely reflecting functional heterogeneity.[16,19,83,84] Prior *in vivo* studies using 2P-microscopy in cortical implantation models (e.g., GL261) demonstrated microglial de-ramification and migration near the tumor bulk.[32–34] However, longitudinal measurements of microglial migration and fine process motility in deep white matter and distant infiltration zones have not been performed. Using 3P microscopy, we quantified microglial fine process dynamics at distant infiltration zones. We identified a marked loss of cellular complexity of microglia, consistent with reports of microglial de-ramification in GB models and human samples.[34,85–89] Microglial density was also increased, consistent with human samples and mouse models.[16] Strikingly, microglial process motility initially increased upon sparse infiltration of GB cells into the CC but declined in densely infiltrated regions. This biphasic response may reflect a transition from an early reactive state to tumor-instructed functional reprogramming.[21,90,91] Our measurements of microglial motility in the GB-infiltrated cortex, however, did not recapitulate this biphasic pattern but instead showed a more uniform reduction of motility under dense infiltration conditions. These data suggest fundamental differences in microglial behavior between the CC and cortex, potentially related to different microenvironments in white and gray matter.[92–94] Our immunocompetent model allowed investigation of microglia-tumor interactions *in vivo*.[53] Although microglial recruitment to the FIZ has been proposed,[26,32] its kinetics remained undefined. Consistent with previous studies reporting only minimal microglial migration in the cortical parenchyma in the absence of pathological stimuli,[11,62,95,96] we also observed very little microglial migration within the non-infiltrated cortex. We found that microglia migrated towards GB cells within a distance of ~150 μm at the FIZ. This fits well with previous studies across different lesion models observing a recruitment radius of microglia between 100–200 μm.[97] Microglial behavior at the FIZ was heterogeneous, consistent with single-cell and spatial transcriptomic studies in GB and other disease contexts.[7,26,83,98,99] We also investigated the molecular underpinnings of microglial recruitment to the FIZ. A potential mechanism involves the CX3CR1-CX3CL1 axis. CX3CR1, the sole receptor for fractalkine (CX3CL1), is a critical regulator of microglial homeostasis, influencing phagocytic activity and migratory behavior.[62,66,67,100,101] GB cells can express and secrete CX3CL1,[102,103] although the consequences of this signaling axis for tumor proliferation and invasion remain incompletely understood. Prior studies on glioma reported divergent outcomes of CX3CR1 deficiency.[104,105] Interestingly, in patients, CX3CR1-reducing polymorphisms that lower receptor function have been linked to prolonged survival.[106,107] Our findings provide additional spatial context by showing that CX3CR1 deficiency in FIZ microglia leads to enhanced microglial migration and increased phagocytic structures. These changes coincide with reduced GB cell velocity and density in line with recent work demonstrating elevated microglial reactivity in CX3CR1-deficient mice, suggesting that enhanced microglial reactivity may constrain GB invasion at distant sites.[67] Our findings indicate that selective alteration of this pathway may modify microglial behavior and limit GB invasion at the FIZ, highlighting CX3CR1 as a potential therapeutic target. Notably, both small-molecule and biologic antagonists of CX3CR1 have been reported.[108,109]

Placing this in a broader therapeutic context, we examined how pharmacological microglial depletion affects GB cell dynamics using the CSF1R inhibitor PLX5622. CSF1R targeting has yielded heterogeneous, context-dependent outcomes across GB models and clinical trials. The landmark study by Pyonteck et al.[74] demonstrated that CSF1R inhibition with BLZ945 reprogrammed microglia and macrophages, resulting in tumor regression and prolonged survival. Additional benefits were reported when CSF1R blockade was combined with VEGFR inhibition (GW2580)[110] or radiotherapy (PLX3397).[111] Yet responses were transient in some proneural models and clinical trials failed to demonstrate clear efficacy, highlighting strong subtype- and context-dependence.[112–119] In our autochthonous mesenchymal GB model, CSF1R inhibition with PLX5622 reduced microglia and coincided with slower GB migration and impaired TM plasticity at the FIZ. Such effects may reflect loss of microglia-derived trophic factors, including TGF-β, IGF-1, and MMP activity. Supporting this idea, microglial TGF-β promotes invasion via MMP-2,[120] whereas Watson et al.[121] showed that CSF1R inhibition can induce TGF-β-driven fibrotic niches that facilitate recurrence. Collectively, these findings indicate that CSF1R targeting may transiently restrain invasion, but the outcome likely depends on tumor subtype and TME context.

Our study provides mechanistic insight into GB cell migration and infiltration dynamics at the FIZ in relation to microglial dynamics in an immunocompetent mouse model. By interfering with microglial function, both pharmacologically and genetically, we show that microglia are important modulators of GB cell migration and TM plasticity.

Limitations of the study

Our work indicates a biphasic microglial surveillance response during increasing GB infiltration at the FIZ; however, the molecular states underlying these functional changes remain undefined. *Cx3cr1*$^{gfp/wt}$ heterozygosity may influence microglial

behavior,[105] and our findings may not generalize to other GB subtypes beyond the mesenchymal model used here. Additional limitations include the restricted genetic complexity of the autochthonous model, which does not recapitulate the broader genetic and epigenetic spectrum of human GB (e.g., MGMT promoter methylation). Postnatal plasmid injection can elicit a transient inflammatory response, typically resolving within ~3 weeks[122]; importantly, longitudinal imaging was performed exclusively in the contralateral hemisphere, spatially separated from the induction site. Finally, variability in penetrance and tumor burden represents a model-inherent constraint yet mirrors human GB heterogeneity.

RESOURCE AVAILABILITY

Lead contact

Requests for further information, resources, and reagents should be directed to and will be fulfilled by the lead contact, Felix C. Nebeling (felix.nebeling@dzne.de).

Materials availability

All unique reagents generated in this study are available from the lead contact with a completed material transfer agreement.

Data and code availability

The authors declare that the data supporting the findings of this study are available within the paper, the STAR Methods section, and supplemental information.

ACKNOWLEDGMENTS

F.N. received funding from the Mildred-Scheel School of Oncology, Cologne-Bonn. This work was supported by DZNE and grants to M.F. and P.S. by the European Union ERC-CoG (MicroSynCom 865618, H3.3Cancer 616744). M.F. received funding from the German Research Foundation DFG (SFB1089 C01, B06; SPP2395) and is a member of the DFG excellence cluster ImmunoSensation2. This work was also supported by iBehave and the CANTAR network to M.F., F.C.N., P.S., and M.H. (funded by the Ministry of Culture and Science of the State of North Rhine-Westphalia; the funders had no role in study design, data collection, and interpretation, or the decision to submit the work for publication). P.S. received funding from Wilhelm Sander Stiftung, Worldwide Cancer Research Fund (WCRF), and the German Cancer Aid-funded THUNDER program. P.S. and D.B. thank the Helmholtz-Gemeinschaft Aging and Metabolic Programming (AMPro) Consortium. We would like to thank present and former members of the P.S. group involved in this work, along with those in the D.B. group, the Core Research Facilities, especially the Light Microscopy Facility (LMF), Services at DZNE, and the DZNE Animal Research Facilities. P.S. is a recipient of an Honorary Professorship at University College London (2023-2027). H.A. is a recipient of a Boehringer Ingelheim Fonds PhD Fellowship. We thank Ute Heuser-Figgemeier and Alexandra Brüggemann from the Institute of Neuropathology, University Hospital Bonn, Bonn, Germany, for their support with tissue processing. We thank Pinzhang Lu for technical assistance. We thank Róisín McManus for careful reading of the manuscript. We thank Julia Steffen, Andrea Baral, and Yvonne Schleehuber for providing technical assistance. We thank P. Thevenaz for developing the ImageJ plugin "stackreg." Figures were prepared with Illustrator CS5 v. 15.0.1 (Adobe) and created with BioRender.com.

AUTHOR CONTRIBUTIONS

F.C.N. conceptualized the experiments, collected data, analyzed data, designed the figures, and wrote the manuscript. F.F. provided technical expertise and support for 3P imaging. F.M. helped analyze microglial motility and carried out image registration. M.M. helped analyze microglia migration and performed PCA. H.A. helped with imaging. N.G. analyzed microglia migration. L.L.F. selected and imaged the human GB samples. S.L. helped with histological analysis. A.D. technically assisted the initial electroporation. M.S. wrote the animal experimental protocol and obtained the license. S.F. provided technical support for the 3P-microscope. D.B. provided funding and reagents. T.P. provided neuropathological samples and expertise. Q.Z. provided PLX5622 and application expertise. S.P. provided the plasmids and helped with technical expertise. M.H. and F.A.G. provided resources and consulting on conceptualization. U.H. provided conceptualization and translational input and helped write the manuscript. P.S. provided conceptualization, technical expertise, and helped write the manuscript. M.F. provided technical expertise, analyzed data, conceptualized experiments, and wrote the manuscript. M.F., P.S., and U.H. supervised the project.

DECLARATION OF INTERESTS

U.H. received advisory board and speaker's honoraria from Medac and Bayer and advisory board honoraria from Servier and OncoMAGNETx Inc. F.A.G. reports travel expenses, stocks, and honoraria from TME Pharma AG; research grants and travel expenses from Elekta AB; grants, research grants, travel expenses, and honoraria from Carl Zeiss Meditec AG; grants, research grants, travel expenses, and honoraria from OncoMAGNETx, Inc.; travel expenses and research grants from Varian Medical Systems, Inc.; travel expenses and/or honoraria from Bristol- Myers Squibb, Cureteq AG, Roche Pharma AG, MSD Sharp and Dohme GmbH, Siemens Healthineers AG, Varian Medical Systems, and AstraZeneca GmbH; non-financial support from Oncare GmbH and Opasca GmbH and patent US10857388B2 together with Carl Zeiss Meditec AG and patent EP4119191A1 with the University of Heidelberg. M.H. reports travel expenses, honoraria for webinars, and research support (consumables) from TME Pharma AG unrelated to this work. M.H. also reports honoraria and clinical advisory board membership from OncoMAGNETx Inc., unrelated to this work.

DECLARATION OF GENERATIVE AI AND AI-ASSISTED TECHNOLOGIES IN THE WRITING PROCESS

During the preparation of this work, the authors used ChatGPT/OpenAI in order to improve readability and identify spelling errors. After using this tool, the authors reviewed and edited the content as needed and take full responsibility for the content of the publication.

STAR★METHODS

Detailed methods are provided in the online version of this paper and include the following:

- KEY RESOURCES TABLE
- METHOD DETAILS
  - Animals
  - *In vivo* electroporation
  - Cranial window surgery
  - Microscope
  - *In vivo* imaging
  - PLX5622 treatment
  - Histology
  - Confocal microscopy
  - Human Samples
- QUANTIFICATION AND STATISTICAL ANALYSIS
  - Microglial motility analysis
  - Migration analysis
  - Tumor microtubes
  - TM Plasticity
  - Principal component analysis
  - Statistics

SUPPLEMENTAL INFORMATION

Supplemental information can be found online at https://doi.org/10.1016/j.immuni.2026.03.010.

Received: October 9, 2024
Revised: September 12, 2025
Accepted: March 11, 2026
Published: March 31, 2026

REFERENCES

1. Ostrom, Q.T., Price, M., Neff, C., Cioffi, G., Waite, K.A., Kruchko, C., and Barnholtz-Sloan, J.S. (2023). CBTRUS Statistical Report: Primary Brain and Other Central Nervous System Tumors Diagnosed in the United States in 2016–2020. Neuro. Oncol *25*, iv1–iv99. https://doi.org/10.1093/neuonc/noad149.
2. Chinot, O.L., Wick, W., Mason, W., Henriksson, R., Saran, F., Nishikawa, R., Carpentier, A.F., Hoang-Xuan, K., Kavan, P., Cernea, D., et al. (2014). Bevacizumab plus radiotherapy-temozolomide for newly diagnosed glioblastoma. N. Engl. J. Med. *370*, 709–722. https://doi.org/10.1056/NEJMoa1308345.
3. Drumm, M.R., Dixit, K.S., Grimm, S., Kumthekar, P., Lukas, R.V., Raizer, J.J., Stupp, R., Chheda, M.G., Kam, K.L., McCord, M., et al. (2020). Extensive brainstem infiltration, not mass effect, is a common feature of end-stage cerebral glioblastomas. Neuro. Oncol *22*, 470–479. https://doi.org/10.1093/neuonc/noz216.
4. Sahm, F., Capper, D., Jeibmann, A., Habel, A., Paulus, W., Troost, D., and von Deimling, A. (2012). Addressing diffuse glioma as a systemic brain disease with single-cell analysis. Arch. Neurol. *69*, 523–526. https://doi.org/10.1001/archneurol.2011.2910.
5. Seker-Polat, F., Pinarbasi Degirmenci, N., Solaroglu, I., and Bagci-Onder, T. (2022). Tumor Cell Infiltration into the Brain in Glioblastoma: From Mechanisms to Clinical Perspectives. Cancers *14*, 443. https://doi.org/10.3390/cancers14020443.
6. Demuth, T., and Berens, M.E. (2004). Molecular mechanisms of glioma cell migration and invasion. J. Neurooncol. *70*, 217–228. https://doi.org/10.1007/s11060-004-2751-6.
7. Garcia-Diaz, C., Pöysti, A., Mereu, E., Clements, M.P., Brooks, L.J., Galvez-Cancino, F., Castillo, S.P., Tang, W., Beattie, G., Courtot, L., et al. (2023). Glioblastoma cell fate is differentially regulated by the microenvironments of the tumor bulk and infiltrative margin. Cell Rep. *42*, 112472. https://doi.org/10.1016/j.celrep.2023.112472.
8. Xiong, H., Wilson, B.A., Ge, X., Gao, X., Cai, Q., Xu, X., Bachoo, R., and Qin, Z. (2024). Glioblastoma Margin as a Diffusion Barrier Revealed by Photoactivation of Plasmonic Nanovesicles. Nano Lett. *24*, 1570–1578. https://doi.org/10.1021/acs.nanolett.3c04101.
9. Bastola, S., Pavlyukov, M.S., Yamashita, D., Ghosh, S., Cho, H., Kagaya, N., Zhang, Z., Minata, M., Lee, Y., Sadahiro, H., et al. (2020). Glioma-initiating cells at tumor edge gain signals from tumor core cells to promote their malignancy. Nat. Commun. *11*, 4660. https://doi.org/10.1038/s41467-020-18189-y.
10. Brooks, L.J., and Parrinello, S. (2017). Vascular regulation of glioma stem-like cells: a balancing act. Curr. Opin. Neurobiol. *47*, 8–15. https://doi.org/10.1016/j.conb.2017.06.008.
11. Damisah, E.C., Hill, R.A., Rai, A., Chen, F., Rothlin, C.V., Ghosh, S., and Grutzendler, J. (2020). Astrocytes and microglia play orchestrated roles and respect phagocytic territories during neuronal corpse removal in vivo. Sci. Adv. *6*, eaba3239. https://doi.org/10.1126/sciadv.aba3239.
12. Glas, M., Rath, B.H., Simon, M., Reinartz, R., Schramme, A., Trageser, D., Eisenreich, R., Leinhaas, A., Keller, M., Schildhaus, H.U., et al. (2010). Residual tumor cells are unique cellular targets in glioblastoma. Ann. Neurol. *68*, 264–269. https://doi.org/10.1002/ana.22036.
13. Venkataramani, V., Yang, Y., Schubert, M.C., Reyhan, E., Tetzlaff, S.K., Wißmann, N., Botz, M., Soyka, S.J., Beretta, C.A., Pramatarov, R.L., et al. (2022). Glioblastoma hijacks neuronal mechanisms for brain invasion. Cell *185*, 2899–2917.e31. https://doi.org/10.1016/j.cell.2022.06.054.
14. Jayaram, M.A., and Phillips, J.J. (2024). Role of the Microenvironment in Glioma Pathogenesis. Annu. Rev. Pathol. *19*, 181–201. https://doi.org/10.1146/annurev-pathmechdis-051122-110348.
15. Yu, K., Hu, Y., Wu, F., Guo, Q., Qian, Z., Hu, W., Chen, J., Wang, K., Fan, X., Wu, X., et al. (2020). Surveying brain tumor heterogeneity by single-cell RNA-sequencing of multi-sector biopsies. Natl. Sci. Rev. *7*, 1306–1318. https://doi.org/10.1093/nsr/nwaa099.
16. Hambardzumyan, D., Gutmann, D.H., and Kettenmann, H. (2016). The role of microglia and macrophages in glioma maintenance and progression. Nat. Neurosci. *19*, 20–27. https://doi.org/10.1038/nn.4185.
17. Simmons, G.W., Pong, W.W., Emnett, R.J., White, C.R., Gianino, S.M., Rodriguez, F.J., and Gutmann, D.H. (2011). Neurofibromatosis-1 heterozygosity increases microglia in a spatially and temporally restricted pattern relevant to mouse optic glioma formation and growth. J. Neuropathol. Exp. Neurol. *70*, 51–62. https://doi.org/10.1097/NEN.0b013e3182032d37.
18. Buonfiglioli, A., and Hambardzumyan, D. (2021). Macrophages and microglia: the cerberus of glioblastoma. Acta Neuropathol. Commun. *9*, 54. https://doi.org/10.1186/s40478-021-01156-z.
19. Gutmann, D.H., and Kettenmann, H. (2019). Microglia/Brain Macrophages as Central Drivers of Brain Tumor Pathobiology. Neuron *104*, 442–449. https://doi.org/10.1016/j.neuron.2019.08.028.
20. Pan, Y., and Monje, M. (2022). Neuron–Glial Interactions in Health and Brain Cancer. Adv. Biol. (Weinh) *6*, e2200122. https://doi.org/10.1002/adbi.202200122.
21. Solomou, G., Young, A.M.H., and Bulstrode, H.J.C.J. (2024). Microglia and macrophages in glioblastoma: landscapes and treatment directions. Mol. Oncol. *18*, 2906–2926. https://doi.org/10.1002/1878-0261.13657.
22. Banerjee, K., Ratzabi, A., Caspit, I.M., Ganon, O., Blinder, P., Jung, S., and Stein, R. (2023). Distinct spatiotemporal features of microglia and monocyte-derived macrophages in glioma. Eur. J. Immunol. *53*, e2250161. https://doi.org/10.1002/eji.202250161.
23. Darmanis, S., Sloan, S.A., Croote, D., Mignardi, M., Chernikova, S., Samghababi, P., Zhang, Y., Neff, N., Kowarsky, M., Caneda, C., et al. (2017). Single-Cell RNA-Seq Analysis of Infiltrating Neoplastic Cells at the Migrating Front of Human Glioblastoma. Cell Rep. *21*, 1399–1410. https://doi.org/10.1016/j.celrep.2017.10.030.
24. Mistry, A.M., Daneshmand, J., Seo, S.J., Lehman, N.L., Miller, D.M., Goodin, D.A., Frieboes, H.B., Chen, J., Masters, A., Williams, B.J., et al. (2024). Spatially Resolved Microglia/Macrophages in Recurrent Glioblastomas Overexpress Fatty Acid Metabolism and Phagocytic Genes. Curr. Oncol. *31*, 1183–1194. https://doi.org/10.3390/curroncol31030088.
25. Müller, S., Kohanbash, G., Liu, S.J., Alvarado, B., Carrera, D., Bhaduri, A., Watchmaker, P.B., Yagnik, G., Di Lullo, E., Malatesta, M., et al. (2017). Single-cell profiling of human gliomas reveals macrophage ontogeny as a basis for regional differences in macrophage activation in the tumor microenvironment. Genome Biol. *18*, 234. https://doi.org/10.1186/s13059-017-1362-4.
26. Yabo, Y.A., Moreno-Sanchez, P.M., Pires-Afonso, Y., Kaoma, T., Nosirov, B., Scafidi, A., Ermini, L., Lipsa, A., Oudin, A., Kyriakis, D., et al. (2024). Glioblastoma-instructed microglia transition to heterogeneous phenotypic states with phagocytic and dendritic cell-like features in patient tumors and patient-derived orthotopic xenografts. Genome Med. *16*, 51. https://doi.org/10.1186/s13073-024-01321-8.
27. Davalos, D., Grutzendler, J., Yang, G., Kim, J.V., Zuo, Y., Jung, S., Littman, D.R., Dustin, M.L., and Gan, W.B. (2005). ATP mediates rapid microglial response to local brain injury in vivo. Nat. Neurosci. *8*, 752–758. https://doi.org/10.1038/nn1472.
28. Nimmerjahn, A., Kirchhoff, F., and Helmchen, F. (2005). Resting microglial cells are highly dynamic surveillants of brain parenchyma in vivo. Science *308*, 1314–1318. https://doi.org/10.1126/science.1110647.
29. Menna, G., Mattogno, P.P., Donzelli, C.M., Lisi, L., Olivi, A., and Della Pepa, G.M. (2022). Glioma-Associated Microglia Characterization in the Glioblastoma Microenvironment through a 'Seed-and Soil' Approach: A Systematic Review. Brain Sci. *12*, 718. https://doi.org/10.3390/brainsci12060718.
30. Cuddapah, V.A., Robel, S., Watkins, S., and Sontheimer, H. (2014). A neurocentric perspective on glioma invasion. Nat. Rev. Neurosci. *15*, 455–465. https://doi.org/10.1038/nrn3765.

31. Vehlow, A., and Cordes, N. (2013). Invasion as target for therapy of glioblastoma multiforme. Biochim. Biophys. Acta *1836*, 236–244. https://doi.org/10.1016/j.bbcan.2013.07.001.

32. Bayerl, S.H., Niesner, R., Cseresnyes, Z., Radbruch, H., Pohlan, J., Brandenburg, S., Czabanka, M.A., and Vajkoczy, P. (2016). Time lapse in vivo microscopy reveals distinct dynamics of microglia-tumor environment interactions-a new role for the tumor perivascular space as highway for trafficking microglia. Glia *64*, 1210–1226. https://doi.org/10.1002/glia.22994.

33. Chen, Z., Ross, J.L., and Hambardzumyan, D. (2019). Intravital 2-photon imaging reveals distinct morphology and infiltrative properties of glioblastoma-associated macrophages. Proc. Natl. Acad. Sci. USA *116*, 14254–14259. https://doi.org/10.1073/pnas.1902366116.

34. Resende, F.F.B., Bai, X., Del Bel, E.A., Kirchhoff, F., Scheller, A., and Titze-de-Almeida, R. (2016). Evaluation of TgH(CX3CR1-EGFP) mice implanted with mCherry-GL261 cells as an in vivo model for morphometrical analysis of glioma-microglia interaction. BMC Cancer *16*, 72. https://doi.org/10.1186/s12885-016-2118-3.

35. Johanns, T.M., Ward, J.P., Miller, C.A., Wilson, C., Kobayashi, D.K., Bender, D., Fu, Y., Alexandrov, A., Mardis, E.R., Artyomov, M.N., et al. (2016). Endogenous Neoantigen-Specific CD8 T Cells Identified in Two Glioblastoma Models Using a Cancer Immunogenomics Approach. Cancer Immunol. Res. *4*, 1007–1015. https://doi.org/10.1158/2326-6066.CIR-16-0156.

36. Hicks, W.H., Bird, C.E., Traylor, J.I., Shi, D.D., El Ahmadieh, T.Y., Richardson, T.E., McBrayer, S.K., and Abdullah, K.G. (2021). Contemporary Mouse Models in Glioma Research. Cells *10*, 712. https://doi.org/10.3390/cells10030712.

37. Filley, A.C., Henriquez, M., and Dey, M. (2017). Recurrent glioma clinical trial, CheckMate-143: the game is not over yet. Oncotarget *8*, 91779–91794. https://doi.org/10.18632/oncotarget.21586.

38. Genoud, V., Marinari, E., Nikolaev, S.I., Castle, J.C., Bukur, V., Dietrich, P.Y., Okada, H., and Walker, P.R. (2018). Responsiveness to anti-PD-1 and anti-CTLA-4 immune checkpoint blockade in SB28 and GL261 mouse glioma models. Oncoimmunology *7*, e1501137. https://doi.org/10.1080/2162402X.2018.1501137.

39. Haddad, A.F., Young, J.S., Amara, D., Berger, M.S., Raleigh, D.R., Aghi, M.K., and Butowski, N.A. (2021). Mouse models of glioblastoma for the evaluation of novel therapeutic strategies. Neurooncol. Adv. *3*, vdab100. https://doi.org/10.1093/noajnl/vdab100.

40. Hardcastle, J., Mills, L., Malo, C.S., Jin, F., Kurokawa, C., Geekiyanage, H., Schroeder, M., Sarkaria, J., Johnson, A.J., and Galanis, E. (2017). Immunovirotherapy with measles virus strains in combination with anti-PD-1 antibody blockade enhances antitumor activity in glioblastoma treatment. Neuro. Oncol *19*, 493–502. https://doi.org/10.1093/neuonc/now179.

41. Wainwright, D.A., Chang, A.L., Dey, M., Balyasnikova, I.V., Kim, C.K., Tobias, A., Cheng, Y., Kim, J.W., Qiao, J., Zhang, L., et al. (2014). Durable therapeutic efficacy utilizing combinatorial blockade against IDO, CTLA-4, and PD-L1 in mice with brain tumors. Clin. Cancer Res. *20*, 5290–5301. https://doi.org/10.1158/1078-0432.CCR-14-0514.

42. Chen, J., Li, Y., Yu, T.S., McKay, R.M., Burns, D.K., Kernie, S.G., and Parada, L.F. (2012). A restricted cell population propagates glioblastoma growth after chemotherapy. Nature *488*, 522–526. https://doi.org/10.1038/nature11287.

43. McNicholas, M., De Cola, A., Bashardanesh, Z., Foss, A., Lloyd, C.B., Hébert, S., Faury, D., Andrade, A.F., Jabado, N., Kleinman, C.L., et al. (2023). A Compendium of Syngeneic, Transplantable Pediatric High-Grade Glioma Models Reveals Subtype-Specific Therapeutic Vulnerabilities. Cancer Discov. *13*, 1592–1615. https://doi.org/10.1158/2159-8290.Cd-23-0004.

44. Pathania, M., De Jay, N., Maestro, N., Harutyunyan, A.S., Nitarska, J., Pahlavan, P., Henderson, S., Mikael, L.G., Richard-Londt, A., Zhang, Y., et al. (2017). H3.3K27M Cooperates with Trp53 Loss and PDGFRA Gain in Mouse Embryonic Neural Progenitor Cells to Induce Invasive High-Grade Gliomas. Cancer Cell *32*, 684–700.e9. https://doi.org/10.1016/j.ccell.2017.09.014.

45. Zuckermann, M., Hovestadt, V., Knobbe-Thomsen, C.B., Zapatka, M., Northcott, P.A., Schramm, K., Belic, J., Jones, D.T.W., Tschida, B., Moriarity, B., et al. (2015). Somatic CRISPR/Cas9-mediated tumour suppressor disruption enables versatile brain tumour modelling. Nat. Commun. *6*, 7391. https://doi.org/10.1038/ncomms8391.

46. Brooks, L.J., Clements, M.P., Burden, J.J., Kocher, D., Richards, L., Devesa, S.C., Zakka, L., Woodberry, M., Ellis, M., Jaunmuktane, Z., et al. (2021). The white matter is a pro-differentiative niche for glioblastoma. Nat. Commun. *12*, 2184. https://doi.org/10.1038/s41467-021-22225-w.

47. Claes, A., Idema, A.J., and Wesseling, P. (2007). Diffuse glioma growth: a guerilla war. Acta Neuropathol. *114*, 443–458. https://doi.org/10.1007/s00401-007-0293-7.

48. Li, Y., Wang, J., Song, S.R., Lv, S.Q., Qin, J.H., and Yu, S.C. (2024). Models for evaluating glioblastoma invasion along white matter tracts. Trends Biotechnol. *42*, 293–309. https://doi.org/10.1016/j.tibtech.2023.09.005.

49. Scherer, H.J. (1938). Structural Development in Gliomas. Am. J. Cancer *34*, 333–351. https://doi.org/10.1158/ajc.1938.333.

50. Takasaki, K., Abbasi-Asl, R., and Waters, J. (2020). Superficial Bound of the Depth Limit of Two-Photon Imaging in Mouse Brain. eNeuro *7*. ENEURO.0255-19.2019. https://doi.org/10.1523/ENEURO.0255-19.2019.

51. Fuhrmann, F., Nebeling, F.C., Musacchio, F., Mittag, M., Poll, S., Müller, M., Ambrad Giovannetti, E., Maibach, M., Schaffran, B., Burnside, E., et al. (2025). Three-photon in vivo imaging of neurons and glia in the medial prefrontal cortex with sub-cellular resolution. Commun. Biol. *8*, 795. https://doi.org/10.1038/s42003-025-08079-8.

52. Horton, N.G., Wang, K., Kobat, D., Clark, C.G., Wise, F.W., Schaffer, C.B., and Xu, C. (2013). In vivo three-photon microscopy of subcortical structures within an intact mouse brain. Nat. Photonics *7*, 205–209. https://doi.org/10.1038/nphoton.2012.336.

53. Schubert, M.C., Soyka, S.J., Tamimi, A., Maus, E., Schroers, J., Wißmann, N., Reyhan, E., Tetzlaff, S.K., Yang, Y., Denninger, R., et al. (2024). Deep intravital brain tumor imaging enabled by tailored three-photon microscopy and analysis. Nat. Commun. *15*, 7383. https://doi.org/10.1038/s41467-024-51432-4.

54. Neftel, C., Laffy, J., Filbin, M.G., Hara, T., Shore, M.E., Rahme, G.J., Richman, A.R., Silverbush, D., Shaw, M.L., Hebert, C.M., et al. (2019). An Integrative Model of Cellular States, Plasticity, and Genetics for Glioblastoma. Cell *178*, 835–849.e21. https://doi.org/10.1016/j.cell.2019.06.024.

55. Aboitiz, F., Scheibel, A.B., Fisher, R.S., and Zaidel, E. (1992). Fiber composition of the human corpus callosum. Brain Res. *598*, 143–153. https://doi.org/10.1016/0006-8993(92)90178-c.

56. Tong, S., Liu, H., Cheng, H., He, C., Du, Y., Zhuang, Z., Qiu, P., and Wang, K. (2019). Deep-brain three-photon microscopy excited at 1600 nm with silicone oil immersion. J. Biophotonics *12*, e201800423. https://doi.org/10.1002/jbio.201800423.

57. Osswald, M., Jung, E., Sahm, F., Solecki, G., Venkataramani, V., Blaes, J., Weil, S., Horstmann, H., Wiestler, B., Syed, M., et al. (2015). Brain tumour cells interconnect to a functional and resistant network. Nature *528*, 93–98. https://doi.org/10.1038/nature16071.

58. Venkataramani, V., Schneider, M., Giordano, F.A., Kuner, T., Wick, W., Herrlinger, U., and Winkler, F. (2022). Disconnecting multicellular networks in brain tumours. Nat. Rev. Cancer *22*, 481–491. https://doi.org/10.1038/s41568-022-00475-0.

59. Strojnik, T., Kavalar, R., Zajc, I., Diamandis, E.P., Oikonomopoulou, K., and Lah, T.T. (2009). Prognostic impact of CD68 and kallikrein 6 in human glioma. Anticancer Res. *29*, 3269–3279.

60. Zhang, J., Li, S., Liu, F., and Yang, K. (2022). Role of CD68 in tumor immunity and prognosis prediction in pan-cancer. Sci. Rep. *12*, 7844. https://doi.org/10.1038/s41598-022-11503-2.

61. Jung, S., Aliberti, J., Graemmel, P., Sunshine, M.J., Kreutzberg, G.W., Sher, A., and Littman, D.R. (2000). Analysis of fractalkine receptor CX(3)CR1 function by targeted deletion and green fluorescent protein reporter gene insertion. Mol. Cell. Biol. *20*, 4106–4114. https://doi.org/10.1128/mcb.20.11.4106-4114.2000.

62. Fuhrmann, M., Bittner, T., Jung, C.K.E., Burgold, S., Page, R.M., Mitteregger, G., Haass, C., LaFerla, F.M., Kretzschmar, H., and Herms, J. (2010). Microglial Cx3cr1 knockout prevents neuron loss in a mouse model of Alzheimer's disease. Nat. Neurosci. *13*, 411–413. https://doi.org/10.1038/nn.2511.

63. Nebeling, F.C., Poll, S., Justus, L.C., Steffen, J., Keppler, K., Mittag, M., and Fuhrmann, M. (2023). Microglial motility is modulated by neuronal activity and correlates with dendritic spine plasticity in the hippocampus of awake mice. eLife *12*, e83176. https://doi.org/10.7554/eLife.83176.

64. Paolicelli, R.C., Sierra, A., Stevens, B., Tremblay, M.E., Aguzzi, A., Ajami, B., Amit, I., Audinat, E., Bechmann, I., Bennett, M., et al. (2022). Microglia states and nomenclature: A field at its crossroads. Neuron *110*, 3458–3483. https://doi.org/10.1016/j.neuron.2022.10.020.

65. Stratoulias, V., Venero, J.L., Tremblay, M.È., and Joseph, B. (2019). Microglial subtypes: diversity within the microglial community. EMBO J. *38*, e101997. https://doi.org/10.15252/embj.2019101997.

66. Cardona, A.E., Pioro, E.P., Sasse, M.E., Kostenko, V., Cardona, S.M., Dijkstra, I.M., Huang, D., Kidd, G., Dombrowski, S., Dutta, R., et al. (2006). Control of microglial neurotoxicity by the fractalkine receptor. Nat. Neurosci. *9*, 917–924. https://doi.org/10.1038/nn1715.

67. Wagner, J., Hoyer, C., Antony, H., Lundgrén, K., Soliymani, R., Crux, S., Justus, L., Keppler, K., Steffen, J., Kurts, C., et al. (2024). CX3CR1 modulates migration of resident microglia towards brain injury. Preprint at bioRxiv. https://doi.org/10.1101/2024.09.23.614458.

68. Möller, K., Brambach, M., Villani, A., Gallo, E., Gilmour, D., and Peri, F. (2022). A role for the centrosome in regulating the rate of neuronal efferocytosis by microglia in vivo. eLife *11*, e82094. https://doi.org/10.7554/eLife.82094.

69. Perez-Pouchoulen, M., VanRyzin, J.W., and McCarthy, M.M. (2015). Morphological and Phagocytic Profile of Microglia in the Developing Rat Cerebellum. eNeuro *2*. ENEURO.0036-15.2015. https://doi.org/10.1523/ENEURO.0036-15.2015.

70. Sierra, A., Encinas, J.M., Deudero, J.J.P., Chancey, J.H., Enikolopov, G., Overstreet-Wadiche, L.S., Tsirka, S.E., and Maletic-Savatic, M. (2010). Microglia shape adult hippocampal neurogenesis through apoptosis-coupled phagocytosis. Cell Stem Cell *7*, 483–495. https://doi.org/10.1016/j.stem.2010.08.014.

71. Tremblay, M.-È., Lowery, R.L., and Majewska, A.K. (2010). Microglial Interactions with Synapses Are Modulated by Visual Experience. PLOS Biol. *8*, e1000527. https://doi.org/10.1371/journal.pbio.1000527.

72. VanRyzin, J.W., Marquardt, A.E., Argue, K.J., Vecchiarelli, H.A., Ashton, S.E., Arambula, S.E., Hill, M.N., and McCarthy, M.M. (2019). Microglial Phagocytosis of Newborn Cells Is Induced by Endocannabinoids and Sculpts Sex Differences in Juvenile Rat Social Play. Neuron *102*, 435–449.e6. https://doi.org/10.1016/j.neuron.2019.02.006.

73. Elmore, M.R.P., Najafi, A.R., Koike, M.A., Dagher, N.N., Spangenberg, E.E., Rice, R.A., Kitazawa, M., Matusow, B., Nguyen, H., West, B.L., et al. (2014). Colony-stimulating factor 1 receptor signaling is necessary for microglia viability, unmasking a microglia progenitor cell in the adult brain. Neuron *82*, 380–397. https://doi.org/10.1016/j.neuron.2014.02.040.

74. Pyonteck, S.M., Akkari, L., Schuhmacher, A.J., Bowman, R.L., Sevenich, L., Quail, D.F., Olson, O.C., Quick, M.L., Huse, J.T., Teijeiro, V., et al. (2013). CSF-1R inhibition alters macrophage polarization and blocks glioma progression. Nat. Med. *19*, 1264–1272. https://doi.org/10.1038/nm.3337.

75. Weil, S., Osswald, M., Solecki, G., Grosch, J., Jung, E., Lemke, D., Ratliff, M., Hänggi, D., Wick, W., and Winkler, F. (2017). Tumor microtubes convey resistance to surgical lesions and chemotherapy in gliomas. Neuro. Oncol *19*, 1316–1326. https://doi.org/10.1093/neuonc/nox070.

76. Bausart, M., Préat, V., and Malfanti, A. (2022). Immunotherapy for glioblastoma: the promise of combination strategies. J. Exp. Clin. Cancer Res. *41*, 35. https://doi.org/10.1186/s13046-022-02251-2.

77. Yu, M.W., and Quail, D.F. (2021). Immunotherapy for Glioblastoma: Current Progress and Challenges. Front. Immunol. *12*, 676301. https://doi.org/10.3389/fimmu.2021.676301.

78. Wang, X., Liang, J., and Sun, H. (2022). The Network of Tumor Microtubes: An Improperly Reactivated Neural Cell Network With Stemness Feature for Resistance and Recurrence in Gliomas. Front. Oncol. *12*, 921975. https://doi.org/10.3389/fonc.2022.921975.

79. Hausmann, D., Hoffmann, D.C., Venkataramani, V., Jung, E., Horschitz, S., Tetzlaff, S.K., Jabali, A., Hai, L., Kessler, T., Azoŕin, D.D., et al. (2023). Autonomous rhythmic activity in glioma networks drives brain tumour growth. Nature *613*, 179–186. https://doi.org/10.1038/s41586-022-05520-4.

80. Weller, J., Potthoff, A.L., Zeyen, T., Schaub, C., Duffy, C., Schneider, M., and Herrlinger, U. (2024). Current status of precision oncology in adult glioblastoma. Mol. Oncol. *18*, 2927–2950. https://doi.org/10.1002/1878-0261.13678.

81. Schneider, M., Vollmer, L., Potthoff, A.L., Ravi, V.M., Evert, B.O., Rahman, M.A., Sarowar, S., Kueckelhaus, J., Will, P., Zurhorst, D., et al. (2021). Meclofenamate causes loss of cellular tethering and decoupling of functional networks in glioblastoma. Neuro. Oncol *23*, 1885–1897. https://doi.org/10.1093/neuonc/noab092.

82. Gritsenko, P.G., Ilina, O., and Friedl, P. (2012). Interstitial guidance of cancer invasion. J. Pathol. *226*, 185–199. https://doi.org/10.1002/path.3031.

83. Sankowski, R., Böttcher, C., Masuda, T., Geirsdottir, L., Sagar, S., Sindram, E., Seredenina, T., Muhs, A., Scheiwe, C., Shah, M.J., et al. (2019). Mapping microglia states in the human brain through the integration of high-dimensional techniques. Nat. Neurosci. *22*, 2098–2110. https://doi.org/10.1038/s41593-019-0532-y.

84. Sankowski, R., Süß, P., Benkendorff, A., Böttcher, C., Fernandez-Zapata, C., Chhatbar, C., Cahueau, J., Monaco, G., Gasull, A.D., Khavaran, A., et al. (2024). Multiomic spatial landscape of innate immune cells at human central nervous system borders. Nat. Med. *30*, 186–198. https://doi.org/10.1038/s41591-023-02673-1.

85. Annovazzi, L., Mellai, M., Bovio, E., Mazzetti, S., Pollo, B., and Schiffer, D. (2018). Microglia immunophenotyping in gliomas. Oncol. Lett. *15*, 998–1006. https://doi.org/10.3892/ol.2017.7386.

86. Chia, K., Mazzolini, J., Mione, M., and Sieger, D. (2018). Tumor initiating cells induce Cxcr4-mediated infiltration of pro-tumoral macrophages into the brain. eLife *7*, e31918. https://doi.org/10.7554/eLife.31918.

87. Kvisten, M., Mikkelsen, V.E., Stensjøen, A.L., Solheim, O., Van Der Want, J., and Torp, S.H. (2019). Microglia and macrophages in human glioblastomas: A morphological and immunohistochemical study. Mol. Clin. Oncol. *11*, 31–36. https://doi.org/10.3892/mco.2019.1856.

88. Mazzolini, J., Le Clerc, S., Morisse, G., Coulonges, C., Zagury, J.F., and Sieger, D. (2022). Wasl is crucial to maintain microglial core activities during glioblastoma initiation stages. Glia *70*, 1027–1051. https://doi.org/10.1002/glia.24154.

89. Ricard, C., Tchoghandjian, A., Luche, H., Grenot, P., Figarella-Branger, D., Rougon, G., Malissen, M., and Debarbieux, F. (2016). Phenotypic dynamics of microglial and monocyte-derived cells in glioblastoma-bearing mice. Sci. Rep. *6*, 26381. https://doi.org/10.1038/srep26381.

90. Karabag, D., Scheiblich, H., Griep, A., Santarelli, F., Schwartz, S., Heneka, M.T., and Ising, C. (2023). Characterizing microglial senescence: Tau as a key player. J. Neurochem. *166*, 517–533. https://doi.org/10.1111/jnc.15866.

91. Qin, J., Ma, Z., Chen, X., and Shu, S. (2023). Microglia activation in central nervous system disorders: A review of recent mechanistic investigations and development efforts. Front. Neurol. *14*, 1103416. https://doi.org/10.3389/fneur.2023.1103416.

92. Grabert, K., Michoel, T., Karavolos, M.H., Clohisey, S., Baillie, J.K., Stevens, M.P., Freeman, T.C., Summers, K.M., and McColl, B.W. (2016). Microglial brain region-dependent diversity and selective regional sensitivities to aging. Nat. Neurosci. *19*, 504–516. https://doi.org/10.1038/nn.4222.

93. Hart, A.D., Wyttenbach, A., Perry, V.H., and Teeling, J.L. (2012). Age related changes in microglial phenotype vary between CNS regions: gray versus white matter differences. Brain Behav. Immun. *26*, 754–765. https://doi.org/10.1016/j.bbi.2011.11.006.

94. van der Poel, M., Ulas, T., Mizee, M.R., Hsiao, C.C., Miedema, S.S.M., Adelia, S.,K.G., Schuurman, K.G., Helder, B., Tas, S.W., Schultze, J.L., et al. (2019). Transcriptional profiling of human microglia reveals grey-white matter heterogeneity and multiple sclerosis-associated changes. Nat. Commun. *10*, 1139. https://doi.org/10.1038/s41467-019-08976-7.

95. Askew, K., Li, K., Olmos-Alonso, A., Garcia-Moreno, F., Liang, Y., Richardson, P., Tipton, T., Chapman, M.A., Riecken, K., Beccari, S., et al. (2017). Coupled Proliferation and Apoptosis Maintain the Rapid Turnover of Microglia in the Adult Brain. Cell Rep. *18*, 391–405. https://doi.org/10.1016/j.celrep.2016.12.041.

96. Boghozian, R., Sharma, S., Narayana, K., Cheema, M., and Brown, C.E. (2023). Sex and interferon gamma signaling regulate microglia migration in the adult mouse cortex in vivo. Proc. Natl. Acad. Sci. USA *120*, e2302892120. https://doi.org/10.1073/pnas.2302892120.

97. Ahn, S.J., Anrather, J., Nishimura, N., and Schaffer, C.B. (2018). Diverse Inflammatory Response After Cerebral Microbleeds Includes Coordinated Microglial Migration and Proliferation. Stroke *49*, 1719–1726. https://doi.org/10.1161/STROKEAHA.117.020461.

98. Ren, Y., Huang, Z., Zhou, L., Xiao, P., Song, J., He, P., Xie, C., Zhou, R., Li, M., Dong, X., et al. (2023). Spatial transcriptomics reveals niche-specific enrichment and vulnerabilities of radial glial stem-like cells in malignant gliomas. Nat. Commun. *14*, 1028. https://doi.org/10.1038/s41467-023-36707-6.

99. Dadwal, S., and Heneka, M.T. (2024). Microglia heterogeneity in health and disease. FEBS Open Bio *14*, 217–229. https://doi.org/10.1002/2211-5463.13735.

100. Lee, S., Varvel, N.H., Konerth, M.E., Xu, G., Cardona, A.E., Ransohoff, R.M., and Lamb, B.T. (2010). CX3CR1 deficiency alters microglial activation and reduces beta-amyloid deposition in two Alzheimer's disease mouse models. Am. J. Pathol. *177*, 2549–2562. https://doi.org/10.2353/ajpath.2010.100265.

101. Liu, Z., Condello, C., Schain, A., Harb, R., and Grutzendler, J. (2010). CX3CR1 in microglia regulates brain amyloid deposition through selective protofibrillar amyloid-β phagocytosis. J. Neurosci. *30*, 17091–17101. https://doi.org/10.1523/jneurosci.4403-10.2010.

102. Erreni, M., Solinas, G., Brescia, P., Osti, D., Zunino, F., Colombo, P., Destro, A., Roncalli, M., Mantovani, A., Draghi, R., et al. (2010). Human glioblastoma tumours and neural cancer stem cells express the chemokine CX3CL1 and its receptor CX3CR1. Eur. J. Cancer *46*, 3383–3392. https://doi.org/10.1016/j.ejca.2010.07.022.

103. Sciumè, G., Soriani, A., Piccoli, M., Frati, L., Santoni, A., and Bernardini, G. (2010). CX3CR1/CX3CL1 axis negatively controls glioma cell invasion and is modulated by transforming growth factor-beta1. Neuro-oncology *12*, 701–710. https://doi.org/10.1093/neuonc/nop076.

104. Liu, C., Luo, D., Streit, W.J., and Harrison, J.K. (2008). CX3CL1 and CX3CR1 in the GL261 murine model of glioma: CX3CR1 deficiency does not impact tumor growth or infiltration of microglia and lymphocytes. J. Neuroimmunol. *198*, 98–105. https://doi.org/10.1016/j.jneuroim.2008.04.016.

105. Feng, X., Szulzewsky, F., Yerevanian, A., Chen, Z., Heinzmann, D., Rasmussen, R.D., Alvarez-Garcia, V., Kim, Y., Wang, B., Tamagno, I., et al. (2015). Loss of CX3CR1 increases accumulation of inflammatory monocytes and promotes gliomagenesis. Oncotarget *6*, 15077–15094. https://doi.org/10.18632/oncotarget.3730.

106. Lee, S., Latha, K., Manyam, G., Yang, Y., Rao, A., and Rao, G. (2020). Role of CX3CR1 signaling in malignant transformation of gliomas. Neuro-oncology *22*, 1463–1473. https://doi.org/10.1093/neuonc/noaa075.

107. Rodero, M., Marie, Y., Coudert, M., Blondet, E., Mokhtari, K., Rousseau, A., Raoul, W., Carpentier, C., Sennlaub, F., Deterre, P., et al. (2008). Polymorphism in the microglial cell-mobilizing CX3CR1 gene is associated with survival in patients with glioblastoma. J. Clin. Oncol. *26*, 5957–5964. https://doi.org/10.1200/JCO.2008.17.2833.

108. Chen, G., Zhou, Z., Sha, W., Wang, L., Yan, F., Yang, X., Qin, X., Wu, M., Li, D., Tian, S., et al. (2020). A novel CX3CR1 inhibitor AZD8797 facilitates early recovery of rat acute spinal cord injury by inhibiting inflammation and apoptosis. Int. J. Mol. Med. *45*, 1373–1384. https://doi.org/10.3892/ijmm.2020.4509.

109. Low, S., Wu, H., Jerath, K., Tibolla, A., Fogal, B., Conrad, R., MacDougall, M., Kerr, S., Berger, V., Dave, R., et al. (2020). VHH antibody targeting the chemokine receptor CX3CR1 inhibits progression of atherosclerosis. mAbs *12*, 1709322. https://doi.org/10.1080/19420862.2019.1709322.

110. Achyut, B.R., Shankar, A., Iskander, A.S., Ara, R., Angara, K., Zeng, P., Knight, R.A., Scicli, A.G., and Arbab, A.S. (2015). Bone marrow derived myeloid cells orchestrate antiangiogenic resistance in glioblastoma through coordinated molecular networks. Cancer Lett. *369*, 416–426. https://doi.org/10.1016/j.canlet.2015.09.004.

111. Stafford, J.H., Hirai, T., Deng, L., Chernikova, S.B., Urata, K., West, B.L., and Brown, J.M. (2016). Colony stimulating factor 1 receptor inhibition delays recurrence of glioblastoma after radiation by altering myeloid cell recruitment and polarization. Neuro. Oncol *18*, 797–806. https://doi.org/10.1093/neuonc/nov272.

112. Butowski, N., Colman, H., De Groot, J.F., Omuro, A.M., Nayak, L., Wen, P.Y., Cloughesy, T.F., Marimuthu, A., Haidar, S., Perry, A., et al. (2016). Orally administered colony stimulating factor 1 receptor inhibitor PLX3397 in recurrent glioblastoma: an Ivy Foundation Early Phase Clinical Trials Consortium phase II study. Neuro. Oncol *18*, 557–564. https://doi.org/10.1093/neuonc/nov245.

113. Liaw, K., Reddy, R., Sharma, A., Li, J., Chang, M., Sharma, R., Salazar, S., Kannan, S., and Kannan, R.M. (2021). Targeted systemic dendrimer delivery of CSF-1R inhibitor to tumor-associated macrophages improves outcomes in orthotopic glioblastoma. Bioeng. Transl. Med. *6*, e10205. https://doi.org/10.1002/btm2.10205.

114. Mendez, J.S., Cohen, A.L., Eckenstein, M., Jensen, R.L., Burt, L.M., Salzman, K.L., Chamberlain, M., Hsu, H.H., Hutchinson, M., Iwamoto, F., et al. (2024). Phase 1b/2 study of orally administered pexidartinib in combination with radiation therapy and temozolomide in patients with newly diagnosed glioblastoma. Neurooncol. Adv. *6*, vdae202. https://doi.org/10.1093/noajnl/vdae202.

115. Pombo Antunes, A.R., Scheyltjens, I., Lodi, F., Messiaen, J., Antoranz, A., Duerinck, J., Kancheva, D., Martens, L., De Vlaminck, K., Van Hove, H., et al. (2021). Single-cell profiling of myeloid cells in glioblastoma across species and disease stage reveals macrophage competition and specialization. Nat. Neurosci. *24*, 595–610. https://doi.org/10.1038/s41593-020-00789-y.

116. Przystal, J.M., Becker, H., Canjuga, D., Tsiami, F., Anderle, N., Keller, A.L., Pohl, A., Ries, C.H., Schmittnaegel, M., Korinetska, N., et al. (2021). Targeting CSF1R Alone or in Combination with PD1 in Experimental Glioma. Exp. Glioma, Cancers (Basel) *13*, 2400. https://doi.org/10.3390/cancers13102400.

117. Quail, D.F., Bowman, R.L., Akkari, L., Quick, M.L., Schuhmacher, A.J., Huse, J.T., Holland, E.C., Sutton, J.C., and Joyce, J.A. (2016). The tumor microenvironment underlies acquired resistance to CSF-1R inhibition in gliomas. Science *352*, aad3018. https://doi.org/10.1126/science.aad3018.

118. Rao, R., Han, R., Ogurek, S., Xue, C., Wu, L.M., Zhang, L., Zhang, L., Hu, J., Phoenix, T.N., Waggoner, S.N., et al. (2022). Glioblastoma genetic drivers dictate the function of tumor-associated macrophages/microglia and responses to CSF1R inhibition. Neuro. Oncol *24*, 584–597. https://doi.org/10.1093/neuonc/noab228.

119. Yan, D., Kowal, J., Akkari, L., Schuhmacher, A.J., Huse, J.T., West, B.L., and Joyce, J.A. (2017). Inhibition of colony stimulating factor-1 receptor abrogates microenvironment-mediated therapeutic resistance in gliomas. Oncogene *36*, 6049–6058. https://doi.org/10.1038/onc.2017.261.

120. Wesolowska, A., Kwiatkowska, A., Slomnicki, L., Dembinski, M., Master, A., Sliwa, M., Franciszkiewicz, K., Chouaib, S., and Kaminska, B. (2008). Microglia-derived TGF-beta as an important regulator of glioblastoma invasion–an inhibition of TGF-beta-dependent effects by shRNA against human TGF-beta type II receptor. Oncogene *27*, 918–930. https://doi.org/10.1038/sj.onc.1210683.

121. Watson, S.S., Zomer, A., Fournier, N., Lourenco, J., Quadroni, M., Chryplewicz, A., Nassiri, S., Aubel, P., Avanthay, S., Croci, D., et al. (2024). Fibrotic response to anti-CSF-1R therapy potentiates glioblastoma recurrence. Cancer Cell *42*, 1507–1527.e11. https://doi.org/10.1016/j.ccell.2024.08.012.

122. Gu, L., Kleiber, S., Schmid, L., Nebeling, F., Chamoun, M., Steffen, J., Wagner, J., and Fuhrmann, M. (2014). Long-term in vivo imaging of dendritic spines in the hippocampus reveals structural plasticity. J. Neurosci. *34*, 13948–13953. https://doi.org/10.1523/JNEUROSCI.1464-14.2014.

123. Giordano, F.A., Layer, J.P., Leonardelli, S., Friker, L.L., Turiello, R., Corvino, D., Zeyen, T., Schaub, C., Müller, W., Sperk, E., et al. (2024). L-RNA aptamer-based CXCL12 inhibition combined with radiotherapy in newly-diagnosed glioblastoma: dose escalation of the phase I/II GLORIA trial. Nat. Commun. *15*, 4210. https://doi.org/10.1038/s41467-024-48416-9.

124. Guizar-Sicairos, M., Thurman, S.T., and Fienup, J.R. (2008). Efficient subpixel image registration algorithms. Opt. Lett. *33*, 156–158. https://doi.org/10.1364/OL.33.000156.

125. van der Walt, S., Schönberger, J.L., Nunez-Iglesias, J., Boulogne, F., Warner, J.D., Yager, N., Gouillart, E., and Yu, T.; scikit-image contributors (2014). scikit-image: image processing in Python. PeerJ *2*, e453. https://doi.org/10.7717/peerj.453.

126. Thévenaz, P., Ruttimann, U.E., and Unser, M. (1998). A pyramid approach to subpixel registration based on intensity. IEEE Trans. Image Process. *7*, 27–41. https://doi.org/10.1109/83.650848.

127. Musacchio, F., Crux, S., Nebeling, F., Gockel, N., Fuhrmann, F., and Fuhrmann, M. (2025). MotilA – A Python pipeline for the analysis of microglial fine process motility in 3D time-lapse multiphoton microscopy data. J. Open Source Softw. *10*, 9267. https://doi.org/10.21105/joss.09267.

STAR★METHODS

KEY RESOURCES TABLE

REAGENT or RESOURCE	SOURCE	IDENTIFIER
Chemicals, peptides, and recombinant proteins		
Buprenorphine	Reckitt Benckiser	
Isoflurane	Virbac	Vetflurane®
Metamizol-Natrium 1 H_2O	Serumwerk Bernburg	Metapyrin, CAS: 68-89-36
Ketamin	Medistar	Ketamin 10% Inj.-Lsg.
Xylacin	Bayer	Rompun®
Texas Red™	ThermoFisher	Cat# 1864
Ki-67 Antibody	Abcam	Cat#16667; RRID: AB_302459
CD11b Antibody	BD Biosciences	Cat#565080;RRID: AB_2722548
CD44 Antibody	BD Biosciences	Cat#558739;RRID: AB_397098
CD68 Antibody	Biolegend	Cat#916104; RRID: AB_2616797
PBase bicistronic construct with SpCas9, PiggyBase under hGFAPmin promoter	Simona Parrinello	N/A
PBvectortdTomato fluorescent reporter, sgRNAs for Nf1, Pten and Trp53.	Simona Parrinello	N/A
Fastgreen	Sigma	Cat#P6148
Critical commercial assays		
Plasmid Mega Kit	Qiagen	Cat#12181
Experimental models: Organisms/strains		
Mus musculus: C57BL/6J	The Jackson Laboratory	Strain #: 0664; RRID:IMSR_JAX:000664
Mus musculus: B6.129P-CX3CR1^{tm1Litt}/J	The Jackson Laboratory	Strain #: 5582; RRID:IMSR_JAX:005582
Software and algorithms		
Fiji	https://fiji.sc/	N/A
Imaris	https://imaris.oxinst.com/	N/A
Python	https://www.python.org/	N/A
GraphPad Prism	https://www.graphpad.com/	N/A
Zen microscope software	https://www.zeiss.com/microscopy/de/home.html	N/A
Biorender	https://biorender.com/	N/A

METHOD DETAILS

Animals

Mice were group-housed and separated by gender with a day/night cycle of 12 hr. Water and food were accessible *ad libitum*. All experiments were performed according to animal care guidelines and approved by the Landesamt für Natur, Umwelt und Verbraucherschutz of North Rhine-Westphalia (Germany) (#81-02.04.2018.A148). C57BL/6J (Stock:000664) were obtained from Jackson Laboratory. CX3CR1-GFP knock-in mice carry the international name: B6.129P-CX3CR1^{tm1Litt}/J (Stock: 5582) Jackson Laboratory. The mouse line expresses eGFP in monocytes, dendritic cells, NK cells, and microglia in the brain. The *Gfp* gene is introduced as a knock-in into the allele of the *Cx3cr1* gene (chemokine C-X3-C motif receptor 1). These mice were first described by Jung et al.[61]

In vivo electroporation

Tumor induction was performed as described before.[7] In short, two separate plasmids were injected into the left ventricle of mice at postnatal day 2 after 60–90 sec of cold-shock immobilization. One plasmid contained the gRNAs for Nf1, Pten and P53 alongside the tdTomato fluorescent reporter under the h_{min}GFAP reporter.[7] The other carried the episomal SpCas9 and the transposase for stable tdTom expression in the transfected NSCs and their progeny. The PiggyBase (0.5 μg/μl) and PiggyBac vectors at a molar ratio of 1:1 were diluted in TE buffer together with 0.1% fast green dye (Sigma) for visual tracing of the injection. Electroporation was performed with 5 square pulses with 50 ms per pulse at U=100V and with 850 msec intervals.

Cranial window surgery

Cortical window surgery was carried out four weeks prior to imaging. Mice were anesthetized with an intraperitoneal (i.p.) injection of ketamine/xylazine (0.13/0.01 mg/g body weight). As an analgesic, mice received buprenorphine (0.1 mg/kg subcutaneously (s.c.), Reckitt Benckiser) shortly before surgery. The body temperature was maintained with a heating pad at 37°C. After fixation in a stereotaxic frame, the skin was removed under aseptic conditions. Using epifluorescence, the location of the bulky tumor was visualized below the left somatosensory cortex and accordingly a craniotomy above the right somatosensory cortex (4 mm diameter) was performed with a dental drill. The dura was carefully removed. The brain surface was rinsed with sterile saline, and #1 coverslips (4 mm diameter) were sealed into the craniotomy with dental cement. Post-surgery, mice received metamizol (200 mg/kg) in the drinking water for 3 consecutive days. For head-fixation during *in vivo* imaging a headpost (Luigs & Neumann) was cemented adjacent to the imaging window.

Microscope

The microscope has recently been described in detail by our group.[51] In short, 3P-excitation is achieved with a wavelength-tunable excitation source from Spectra Physics (NOPA, Spectra Physics) pumped by a femtosecond laser (Spirit, Spectra Physics). The laser repetition rate is maintained at 2 MHz. The 2P excitation source is a Ti:sapphire laser (Chameleon Ultra II, Coherent). The laser repetition rate is at 80 MHz. Images are taken with a multiphoton microscope built of a Thorlabs microscope base (EMB100/M) and primary scan path optics with 900–1900 nm coatings. Two GaAsP photomultiplier tubes (PMT2100, BDM3214-3P, Thorlabs) are used for non-descanned detection. ThorImage (Version 4.3, Thorlabs) is used to control imaging parameters. A 25x water immersion microscope objective with the numerical aperture of 1.05 (XLPLN25XWMP2, Olympus) is used. Green and red signals are separated by a 488 nm dichroic mirror (Di02-R488, Semrock) and 562 nm dichroic mirror (FF562-Di03). Then the eGFP and third harmonic generated (THG) signals are further filtered by a 525/50 nm band-pass filter (FF03-525/ 50, Semrock) and 447/60 nm (FF02-447/ 60, Semrock) band-pass filter, respectively. Lateral movements are done with the 2D stepper motor (PLS-XY, Thorlabs), z-stacks are acquired using the built-in z-axis motor or a piezo focus device (PFM450, Thorlabs).

In vivo imaging

Mice were anesthetized with isoflurane (1% in 0.7l O_2/min.) and head-fixed under the microscope on a heating pad at 37°C. Deep overview *in vivo* z-stacks were recorded with depth increments of 7 μm and 0.65 μm/pixel resolution and 1.49 μs pixel dwell time. Z-stacks spanned 900–1100 μm from the pial surface through the somatosensory cortex and CC. For visualization of CC and tdTom+ GB cells excitation wavelengths of λ_{Ex}=1650nm was used. Microglia (CX3CR1-GFP) and GB cells (tdTomato) were co-imaged using λ_{Ex}=1300nm. For the measurement of microglial fine process motility, z-stacks of 166.4x166.4x130–150 μm were acquired at 5 μm depth increments, 0.162 μm/pixel, 0.99 μs or 1.49 μs dwell time and with a 5-minute time-interval between z-stacks for a period of 25–30 minutes. Measurements of TM plasticity were performed by acquiring image stacks of 332 × 332 × 150–300 μm at a resolution of 0.325 μm/pixel, with a dwell time of 1.49 μs and a z-step size of 5 μm. Repeated z-stacks were collected every 10 minutes for at least 12 consecutive time points.

PLX5622 treatment

Mice were treated with the CSF1R inhibitor PLX5622 (1200 mg/kg diet; equivalent to1200 ppm; Research Diets, Inc.), formulated in a Poloxamer407–DMSO vehicle and incorporated into a standard AIN-76A rodent diet. Control animals received matched chow containing vehicle alone. Animals had ad libitum access to chow, which was exchanged every 2–3 days. Food intake was monitored by weighing chow at each exchange to confirm sufficient consumption, and male mice were single-housed to avoid dominance effects on food intake.

Histology

Mice were deeply anesthetized with an i.p. injection of ketamine/xylazine and transcardially *perfused* with saline followed by either 4% paraformaldehyde (PFA) or directly fresh frozen at -80°C after extracting the brain. For visualization of the tumor anatomy and infiltration, brains were cut into 70 μm thick coronal slices. The tdTomato from the Piggybac system remained clearly visible without counterstaining. During tissue permeabilization (0.5% Triton-X100, 1h), DAPI was added to the free floating sections for 30 minutes (1:10000). For the visualization of CD44, CD11b and Ki67, coronal 70 μm slices were permeabilized (0.5% Triton-X100, 1h) and subsequently incubated with the respective antibodies (CD44, CD11b, Ki67) in a blocking reagent (4% normal goat serum, 0.4% Triton, and 4% BSA in PBS) over night at room temperature. After washing the samples three times with PBS, secondary antibodies were administered (Alexa Fluor 647, A21235, Alexa Fluor 594, A11058, Alexa Fluor 488, A48262) in 5% normal goat serum/BSA and incubated for 2h at room temperature. During the last 15 minutes of incubation DAPI was added (5mg/ml, 1:10000). Afterward slices were washed three times with PBS, mounted with Dako Mounting Medium, and covered with a glass cover-slip.

Confocal microscopy

For the visualization of GB cell infiltration patterns LSM800 microscope (Zeiss) was used. Entire coronal PFA-fixed brain slices of 70 μm thickness were imaged using a 20x Objective, with a lateral resolution of 0.624 μm/pixel. DAPI- (EX: G 365, dichroic: FT 395, EM: BP 445/50), tdTomato (EX 561/10, dichroic: 573, EM: 600/50) filter-sets were used.

Human Samples

Human pretreatment GB samples were derived from Patients within the GLORIA Trial[123] (SNOXA12C401, 2018-004064-62, NCT04121455) including patients with newly diagnosed, histologically confirmed, supratentorial CNS WHO grade 4 GBs, MGMT promoter methylated.

QUANTIFICATION AND STATISTICAL ANALYSIS

Microglial motility analysis

In general, microglial motility was analyzed as described before.[62,63] In short, stacks were initially rigidly registered using subpixel image registration by cross-correlation[124] provided by the open-source python image processing library Scikit-image.[125] Individual stacks were then median filtered and individual microglia were identified by scrolling through the stacks at each time point and cropped using ImageJ. Z-stacks spanning 35 μm in depth were isolated from the original z-stack. Stacks were registered by applying the ImageJ 'StackReg' plugin.[126] For all time points, the average intensity projections were calculated, resulting in a 2D visualization of microglia and their fine processes. Individual 2D images were merged into a stack. Time points were pseudo colored in red and green. Red areas account for lost, green for gained and yellow for stable microglial fine processes. The turnover rate (TOR) of individual microglia processes was calculated as the number (absolute pixel value) of lost, N_{lost} (red), and newly gained, N_{gained} (green) pixels divided by the sum of all pixels within a determined region of interest (ROI). Building up on these manual analyses we implemented a custom analysis pipeline for automated quantification written in Python as described before[51,127]; in summary, we calculated the temporal variation $\Delta B(t_i)$ of binarized images by subtracting the binarized image $B(t_{i+1})$ at time point t_{i+1} from the binarized image $B(t_i)$ at time point t_i: $\Delta B(t_i) = 2 \times B(t_{i+1}) - B(t_i)$ for $i=0, 1, 2, \ldots, N-1$, where N is the total number of all time lapse time points. Pixels in $\Delta B(t_i)$, that have the value 1, were categorized as stable pixels, whereas pixels with the value -1 were categorized as gained pixels, and pixels with the value 2 as lost pixels. The microglial fine process motility was then assessed by calculating the turnover rate (TOR) as the ratio of the number of all gained pixels $N_g(t_i)$ and all lost pixels $N_l(t_i)$ divided by the sum of all pixels: $TOR(t_i) = (N_g(t_i) + N_l(t_i)) / (N_s(t_i) + N_g(t_i) + N_l(t_i))$, where $N_s(t_i)$ is the number of all stable pixels. The average turnover rate $\overline{TOR}$ was calculated by averaging $TOR(t_i)$ over all $N-1$ time lapse time points.

Migration analysis

Motion correction of the 4D imaging data (3D spatial volumes over time) was performed by rigid-body registration. Each time point was aligned to a fixed reference volume (stack 0) using phase cross-correlation with subpixel precision[124] as implemented in the Python package scikit-image.[125] Migration of microglia and GB cells was tracked using the "Spots" function in Imaris (Oxford Instruments). Sub-volumes of approximately 100 μm thickness were defined either (1) spanning the entire XY dimension within non-infiltrated and infiltrated regions of cortex and CC, or (2) spanning the full Z-axis while restricted to 100 μm in the XY plane. All analyses were performed in 3D without projection. Cells were manually annotated at the first time point and tracked over time using the autoregressive motion algorithm implemented in Imaris. The maximum gap size was set to 0 and gap closing was disabled. Estimated cell diameters were set to 7 μm for microglia and 12 μm for GB cells to optimize spot detection. Only cells that could be continuously tracked throughout the entire imaging interval were included in the analysis. Cells entering or leaving the imaging volume during acquisition were excluded. For each tracked cell, 3D spatial coordinates (x, y, z) were extracted at each time point. Traveled distance was calculated as the cumulative 3D path length along the reconstructed trajectory. Mean velocity was defined as total 3D path length divided by total tracking time. For proximity analyses, exported coordinates were processed in Python. Euclidean distances were computed in 3D space. Nearest-neighbor distance was defined as the minimal Euclidean distance to the closest GB cell (for microglial analyses) or to the closest cell of the same population (for spatial organization analyses), excluding the reference cell itself. Migration directionality toward GB cells was quantified as the change in Euclidean distance between consecutive time points, calculated as $\Delta d = d(t) - d(t+1)$. Positive Δ-distance values therefore indicate movement toward GB cells, whereas negative values indicate movement away from tumor cells.

Tumor microtubes

Cellular protrusions were classified as previously described.[13] TMs were defined as between 1.25–3 μm thick and with a length of at least 10 μm. TM length and diameter were manually measured in ImageJ (Fiji) on individual optical sections of three-photon z-stacks.

TM Plasticity

Tumor microtube (TM) plasticity was quantified analogously to microglial fine process turnover using a pixel-based approach. Time-lapse image series consisted of approximately 12 consecutive z-stacks acquired at 10-minute intervals. Stacks were first motion-corrected as described above. For analysis, individual GB cells were manually cropped in 3D from the motion-corrected z-stacks to exclude neighboring tumor cells and restrict analysis to single-cell TM structures, with cropping confined to a depth of 35 μm (7 contiguous optical sections at 5 μm z-steps). Subsequent processing and analysis were performed using the MotilA analysis pipeline.[127] Cropped volumes were projected as maximum intensity projections, binarized by intensity thresholding to segment TM structures, and analyzed for temporal variation between consecutive time points by subtraction of binarized images as described for

microglial process turnover. Pixels present at both time points were classified as stable segments, pixels appearing at the later time point as gained segments, and pixels disappearing between time points as lost segments. TM turnover rate for each interval was calculated as:

$$\text{TM turnover}(t_i) = (N\text{gained}(t_i) + N\text{lost}(t_i)) / (N\text{stable}(t_i) + N\text{gained}(t_i) + N\text{lost}(t_i))$$

where N_{stable}, N_{gained}, and N_{lost} represent the number of pixels classified in each category between consecutive time points. The average TM turnover per imaging session was calculated by averaging turnover values across all consecutive intervals.

Principal component analysis

For the clustering analysis, tools from Pythons scikit-learn library were used. First, the data was standardized using scikit-learns StandardScaler algorithm. Principal component analysis was performed in order to decrease the number of feature dimensions. The first four principal components (PC) accounted for over 75% of the variance. Agglomerative clustering was performed, using the Euclidean metric and the linkage criterion 'ward'.

Statistics

Quantifications, statistical analysis, and graph preparation were carried out using GraphPad Prism 9 (GraphPad Software Inc, La Jolla, CA, USA). To test for normal distribution of data, d'agostino and Pearson omnibus normality test was used for sample sizes of $n>6$ and the Shapiro-Wilk normality test for $n<6$. For comparisons between two normally distributed datasets, paired or unpaired two-tailed Student's *t* tests were applied. If no normal distribution was evident, Mann-Whitney test for groups of two was used. One-way ANOVA with Tukey's or Bonferroni's multiple comparison test were performed on data sets larger than two, if normally distributed. For comparison of more than two not normally distributed data sets the Kruskal-Wallis test was performed with Dunn's correction for multiple comparisons. If not indicated differently, data are represented as mean ± SEM.